Does the Operation of a Reservoir Alter Its Interactions with the Atmosphere? Investigating the Role of Advective Fluxes on Energy and Hydrological Balances of the Romaine-2 Subarctic Hydropower Reservoir

ADRIEN PIERRE,[a,b] DANIEL F. NADEAU,[a,b] ANTOINE THIBOULT,[a,b] ALAIN N. ROUSSEAU,[c] FRANÇOIS ANCTIL,[a,b] CHARLES P. DEBLOIS,[d] MAUD DEMARTY,[d] PIERRE-ERIK ISABELLE,[a,b] AND ALAIN TREMBLAY[e]

[a] *Department of Civil and Water Engineering, Université Laval, Quebec, Canada*
[b] *CentrEau–Water Research Centre, Université Laval, Quebec, Canada*
[c] *Institut National de la Recherche Scientifique–Centre Eau Terre Environnement, Quebec, Canada*
[d] *Aqua Consult, Montréal, Quebec, Canada*
[e] *Hydro-Québec, Montréal, Quebec, Canada*

(Manuscript received 31 August 2023, in final form 8 January 2024, accepted 10 January 2024)

ABSTRACT: The hydrological processes of cascading hydroelectric reservoirs differ from those of lakes, due to the importance of the inflows and outflows that vary with energy demand. These heat and water advection terms are rarely considered in water body energy balance analyses even though reservoirs are common man-made structures, especially in North America, and thus may affect the regional climate. This study provides a comprehensive assessment of the water and energy balance of the 85-km^2 Romaine-2 northern reservoir (50.69°N, 63.24°W), mean depth of 44 m, highlighting the significant contribution of the advection heat fluxes. The water balance input was primarily controlled by upstream (turbine) inflows (77.6%), while lateral (natural) inflows and direct precipitation represented 21.2% and 1.2%, respectively. As for the reservoir's heat budget, the net advection of heat accounted on average for 25.0% of the input, of which net radiation was the largest component (73.3%). After accounting for the absence of energy balance closure, latent heat and sensible heat fluxes represented 73.2% and 25.1% of total energy output from the reservoir, respectively. The thermal regime was influenced by the hydrological flow conditions, which were regulated by reservoir management. This played a major role in the evolution of the thermocline and the temperature of the epilimnion, and ultimately, in the dynamics of the turbulent heat fluxes. This study suggests that the heat advection term represents a large fraction of the heat budget of northern reservoirs and should be properly considered.

KEYWORDS: Thermocline; Boreal meteorology; Heat budgets/fluxes; Surface fluxes; Water budget/balance

1. Introduction

Lakes and reservoirs have significantly different radiative and thermal properties than the surrounding land surfaces (Subin et al. 2012). Their energy balance modulates their impact on the local climate. For example, the ability of reservoirs to store net radiation delays the release of heat to the atmosphere (Leppäranta et al. 2016; Schmid and Read 2022). The energy balance also controls the surface temperature of the reservoirs and thus the sensible and latent heat fluxes (Blanken et al. 2011; Momii and Ito 2008). The energy balance also determines the onset/disappearance of ice cover (Cheng et al. 2021; Leppäranta et al. 2019), with direct consequences on the surface albedo (Kirillin et al. 2012) and the rate of greenhouse gas emissions (Denfeld et al. 2018; Jammet et al. 2015). Several studies have attempted to integrate the effects of open water bodies into regional and global climate models, focusing on moisture, heat, and momentum fluxes (MacKay 2012; MacKay et al. 2009; Nazemi and Wheater 2015). However, the contribution of advective fluxes (Rodríguez-Rodríguez and Moreno-Ostos 2006), which remains a fundamental aspect in the study of water bodies mass and energy balances, is often neglected due to the lack of direct measurements. Yet, some studies have confirmed the need to consider these terms in regional climate modeling. Almeida et al. (2022) stated that it is critical to adequately model lateral heat and mass inputs/outputs to reservoirs, as well as water levels for the benefit of climate modeling.

Hydropower reservoirs differ from lakes in that their water level and residence time are largely controlled by human intervention over the course of the year. As a result, their thermal regime can also differ substantially from that of a natural lake. For example, fluctuations in reservoir temperature profiles can be triggered by internal currents resulting from turbine operation, thereby attenuating thermal stratification (Çalışkan and Elçi 2009; Olsson 2022). In addition, large water level fluctuations can induce shoreline transformation and erosion, which increase turbidity (Dirnberger and Weinberger 2005), reduce light penetration, strengthen stratification, and ultimately enhance heat exchanges with the atmosphere (Heiskanen et al. 2015; Saros et al. 2016). Depending on geographic location, regional climate, and hydroelectric demand, reservoirs have specific characteristics that affect their thermal energy and water balances. At mid- and high latitudes, ice and snow cover reservoirs and their watersheds for several months of the year, reducing inflows from shoreline

Supplemental information related to this paper is available at the Journals Online website: https://doi.org/10.1175/JHM-D-23-0149.s1.

Corresponding author: Adrien Pierre, Adrien.pierre.1@ulaval.ca

DOI: 10.1175/JHM-D-23-0149.1

© 2024 American Meteorological Society. This published article is licensed under the terms of the default AMS reuse license. For information regarding reuse of this content and general copyright information, consult the AMS Copyright Policy (www.ametsoc.org/PUBSReuseLicenses).

Brought to you by I.N.R.S. | Unauthenticated | Downloaded 03/14/24 01:14 PM UTC

hillslopes, as well as suppressing heat exchanges with the atmosphere. High winter energy demand from human activities, especially for home heating, requires substantial water release, which in turn lowers reservoir levels. During the spring freshet, reservoir inflows increase, sharply raising water levels. The management of reservoirs alters the seasonality of streamflow, which sets them apart from lakes. Moreover, such water inflows and outflows can represent a significant contribution to the reservoir's energy balance, and thus affect their interactions with the atmosphere. Studies on energy balance of water bodies have been conducted in various regions of the world including high latitudes (Leppäranta et al. 2016; Ragotzkie and Likens 1964), tropical and equatorial regions (MacIntyre et al. 2014; Vallet-Coulomb et al. 2001), and high altitudes (Rodríguez-Rodríguez et al. 2004), but almost exclusively on lakes and rarely on reservoirs.

Net advective fluxes are driven by heat carried by net water flows, which, in the case of a cascade of reservoirs, include upstream inflows (natural or turbined/discharged) and downstream outflows (through spillways and turbines). From a thermodynamic point of view, to obtain the net advection flux, we need to take the sum of the products of the inflows/outflow and the associated water temperatures (Han and Wright 2022; Venkateshan 2021). Therefore, it is impossible to consider the energy balance of a reservoir without including a water balance. In the absence of direct measurements, lateral contributions are estimated using proxies or empirical relationships. For example, to estimate lateral inputs, several studies have relied on relationships with atmospheric predictors such as mean sea level pressure, air and dewpoint temperatures, and wind speed (George et al. 2019), precipitation, and soil moisture (Long et al. 2019), or multiple linear regression models with wavelet and bootstrap techniques (Bashir et al. 2019). Some rare studies have quantified lake inflows and outflows using direct measurements (Leach et al. 2021), but, to the best of our knowledge, this is rare for a reservoir, in part because turbine flow data are often undisclosed by operators. As a result, studies are typically conducted on a one-dimensional basis, neglecting lateral inflows and energy fluxes (e.g., Elo 2007; Momii and Ito 2008; Kallel et al. 2024). Conducting a full water balance of a hydropower reservoir can help quantify and verify the importance of advection terms in the thermal energy balance, particularly when compared to surface turbulent heat fluxes (Xing et al. 2012). In one of the only studies that have considered lateral inputs, Moreno-Ostos et al. (2008) showed that the thermal dynamics of the Sau reservoir in Spain (mean depth of 25 m) were controlled by the advection fluxes induced by water management. Xing et al. (2012) showed that inflow advective heat fluxes of a shallow tropical reservoir were a critical component of the heat budget, with a magnitude equivalent to 71% of the net radiation budget. On the other end, Winter et al. (2003) highlighted that energy advected by precipitation and streams into Mirror Lake (a 49-ha lake in New Hampshire) had little effect on the measured evaporation rates.

The annual heat budgets of water bodies (mostly lakes) were initially measured using simple instruments such as evaporation pans, resistance thermometers, and pyrheliometers (Juday 1940; Saur and Anderson 1956). As a result, early analyses were subject to considerable uncertainties that often led to misinterpretations. More recently, flux (eddy covariance) towers have improved our understanding of the thermal energy balance of water bodies (Metzger et al. 2018; Nordbo et al. 2011; Wilson et al. 2002). Thus, using net radiometers and eddy covariance instruments is now standard practice for measuring surface heat fluxes (Blanken et al. 2000; Rouse et al. 2003, 2005). However, assessing the thermal energy balance of a water body remains complex. First, eddy-covariance-based fluxes suffer from edge effects when taken from the shore—some studies have circumvented this issue by using rafts to deploy instruments on water (Spank et al. 2020; Spence et al. 2003). Second, the oscillations of the measurement system associated with raft motions caused by waves contaminate the recorded data. This can be corrected by using the raft motion data obtained with an accelerometer (Miller et al. 2008; Pierre et al. 2023). Finally, the footprint of the turbulent heat flux measurement tends to differ from that of the other energy balance terms, preventing the thermal energy balance from closing (Pierre et al. 2022).

Studies on the energy balance of deep cascade reservoirs in northern environments are still lacking, and the goal of this paper is to fill this gap through the assessment of (i) the hydrological and thermal energy balances of a midlatitude hydroelectric reservoir at monthly and annual scales, including a thermal regime analysis, characterized by two mixing periods and two stratification periods; (ii) the closure of the energy balance, using direct measurements of the majority of the terms, identifying the dominant processes and the main sources of uncertainty; and (iii) the effect of reservoir management (advective fluxes, water levels) on the thermal regime.

2. Methods

a. Research site

The research site is located at the southern end of the Romaine-2 hydropower reservoir (50.68°N, 63.25°W) in eastern Quebec, Canada [see Fig. 1 in Pierre et al. (2023)], and is characterized by a subarctic Dfc climate (Beck et al. 2018). The 640-MW hydropower reservoir is operated by Hydro-Québec, the provincial government–owned power utility. It is part of the La Romaine hydroelectric complex, which consists of four cascade reservoirs (from Romaine-4 upstream to Romaine-1 downstream) with a full power capacity of 1550 MW (Hydro-Québec 2007). Each reservoir includes a penstock that delivers water to the hydropower plant and a spillway. The Romaine-2 and Romaine-3 penstocks are located at depths of 40 and 35 m, respectively. The inflows into the Romaine-2 reservoir include the upstream inflow of the Romaine-3 reservoir outflow, the lateral inflow consisting of three rivers (Bernard, L'Abbé-Huard, and Mista) and more than 60 small tributaries. The Romaine-2 reservoir discharges into the Romaine-1 reservoir via the Romaine River.

The Romaine-2 and Romaine-3 reservoirs were flooded in 2014 and 2017, respectively. The Romaine-2 reservoir has a

Brought to you by I.N.R.S. | Unauthenticated | Downloaded 03/14/24 01:14 PM UTC

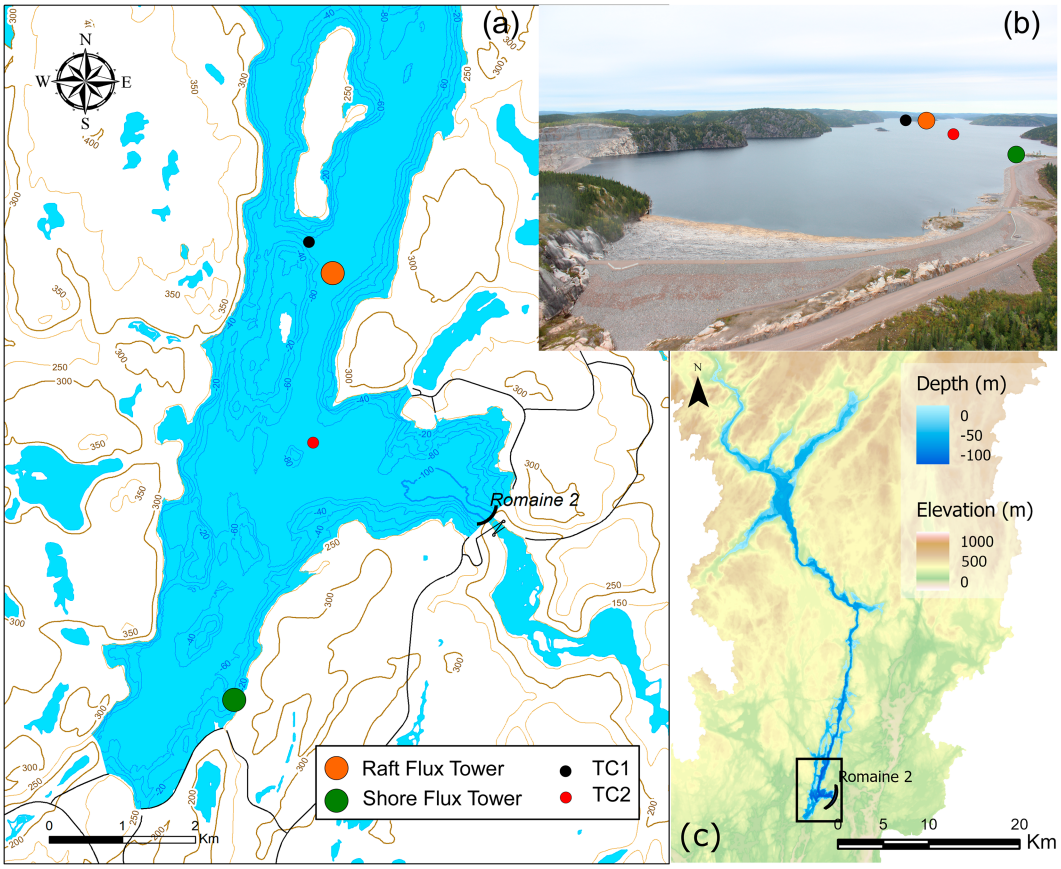

FIG. 1. (a) Location of the southern end of Romaine-2 reservoir [blue and brown isolines represent bathymetry (m) and topography (m MSL), respectively]. (b) Southern edge of the Romaine-2 reservoir with the locations of the experimental setup. (c) Overview of the entire Romaine-2 reservoir with bathymetry in blue and topography in other colors; the black rectangle indicates the area represented in (a). TC refers to the thermistor chains.

maximum surface area of 85.6 km^2, with a mean depth of 44 m, and a maximum depth of 101 m (Fig. 1). It is typically ice-free from May to December, with a mean annual water level fluctuation of 14 m. The catchment area upstream of Romaine-2 reservoir has a surface area of 9987 km^2, which represents 70% of the total catchment area of the Romaine River. More details about the study site can be found in Pierre et al. (2022). The study period extended from 27 June 2018 to 31 December 2022.

b. Energy budget

1) TURBULENT HEAT FLUXES

Turbulent heat fluxes, namely, sensible (H) and latent (LE) heat fluxes (W m^{-2}), were measured using two flux towers. One flux tower was located on the reservoir shore and the other on a 3 m × 3 m raft on the reservoir, deployed each year from early June to mid-October (Fig. 1a). Both towers included an eddy covariance (EC) setup consisting of a fast-response sonic anemometer with an infrared gas analyzer (IRGASON, Campbell Scientific, United States), sampled at a frequency of 10 Hz. A full description of the EC system can be found in Pierre et al. (2022). The fluxes H and LE were calculated as follows:

$$H = \rho_a c_{pa} \overline{w'T'}, \quad \text{and} \tag{1}$$

$$\mathrm{LE} = \lambda_v \rho_a \overline{w'q'}, \tag{2}$$

where ρ_a is the moist air density (kg m^{-3}), c_{pa} is the specific heat of moist air (J kg^{-1} K^{-1}), λ_v is the latent heat of vaporization (J kg^{-1}), T is the air temperature (K), and q is the specific humidity of air (kg kg^{-1}). Here, primes denote fluctuations from the 30-min average, indicated by an overbar. The measuring height of the instruments was 2 m for the raft, while it varied between 11 and 28 m for the shore tower depending on the water level. At the shore station, only data corresponding to winds coming from the reservoir were considered in the analysis.

An accelerometer [attitude and heading reference system (AHRS); Lord Sensing MicroStrain, United States] installed near the IRGASON recorded raft oscillations by capturing all linear acceleration components, angular velocities and the three Euler angles at a frequency of 10 Hz. Raw data were corrected following Miller et al. (2008). Then, the data were

Brought to you by I.N.R.S. | Unauthenticated | Downloaded 03/14/24 01:14 PM UTC

processed using EddyPro (R) software, version 7.0 (LI-COR Biosciences, United States). Flux time series of the raft and shore stations were subsequently merged according to the best quality criteria of Mauder et al. (2013). More details on the EC data processing can be found in Pierre et al. (2023). Overall, 43% of the turbulent heat flux data had to be gap filled: most of the missing fluxes were in winter, when raft data were not available. The dataset was gap filled using a marginal distribution sampling approach (Reichstein et al. 2005).

2) Net radiation

One net radiometer (CNR4, Kipp and Zonen, The Netherlands) was deployed at each station and measured the four components of the net radiation R_n (W m^{-2}):

$$R_n = R_{S\downarrow} - R_{S\uparrow} + R_{L\downarrow} - R_{L\uparrow}, \tag{3}$$

where $R_{S\downarrow}$ and $R_{S\uparrow}$ are shortwave incoming and outgoing radiation components, respectively; and $R_{L\downarrow}$ and $R_{L\uparrow}$ longwave downward and upward radiation components, respectively. To obtain a continuous annual time series of net radiation over the water surface, we combined the following datasets: net radiation measured from the raft from June to October, net radiation measured from the shore during periods of reservoir freeze-up, assuming equivalent winter conditions on the shore and on the reservoir (similar snow cover). During the transition periods (late April–early June and late October–December), incoming radiation fluxes were taken from the shore site, the reflected shortwave radiation from the reservoir was based on the albedo calculated from Patel and Rix (2019), and the emitted longwave radiation was estimated from the Stefan–Boltzmann law considering a surface water temperature estimated from the 0.2-m-deep sensor deployed on the meteorological raft described in more detail below. A water emissivity of 0.99 was used because it provided the best comparison between the raft net radiometer measurements and the empirical Stefan–Boltzmann law using the water surface temperature in open water. Since solar radiation was absorbed in the first few meters of the water column, we could neglect its absorption by bottom sediments. In winter, only a very weak fraction of shortwave radiation entered the water column. Indeed, the high albedo of the ice and snow cover lowered net radiation, while the absorbed incoming radiation by the underlying water decreased due to the above ice–snow layer.

3) Thermal regime

(i) Water temperature

Temperature profiles were measured using two thermistor chains (HOBO TidBit UTBI-001, Onset, United States; Fig. 1a), providing high-resolution data near the surface and lower resolution data at greater depths. More precisely, sensors were spaced 0.2 m apart from the surface to 1 m deep, 0.4 m from 1 to 3 m, 1 m from 3 to 10 m, 2.5 m from 10 to 32.5 m, 8.5 m from 32.5 to 40 m, and 10 m from 40 to 70 m. The first chain, TC1 (Fig. 1), was 15 m long and was deployed in a 30-m-deep zone of the reservoir between two islands. The second chain, TC2 (Fig. 1), was 70 m-long and was deployed in a 100-m-deep area of the reservoir, 1 km south of TC1. The chains were deployed to withstand water level fluctuations. The surface temperature sensors were shielded from solar radiation by a piece of white polystyrene floating on the surface. The observations from the two thermistor chains were averaged for each measurement level to produce a single dataset. Pressure sensors (HOBO water level logger u20-001-03, Onset, Canada) were attached to the chains to confirm that they remained vertical and that the sensors were at their nominal depth. To monitor the presence of the ice cover, time-lapse images of Romaine-2 were also taken on an hourly basis using automated cameras (Reconyx HP2X, United States).

We removed the data when the chain was not vertical or when suspicious temperature spikes were observed. Spikes were defined as a temperature difference of more than 5°C over a two-day period or a difference of more than 2°C over a 12-h period. Then, gaps were filled with several techniques applied in the following order: (i) water surface temperature was derived from linear regression with lower sensors, (ii) water temperature were derived from a linear regression with temperature above and below target, (iii) remaining missing data were filled with yearly mean temperature to which a linear detrending was applied to ensure reconnection with measurements at both ends of the gap, and (iv) remaining missing data were filled with linear interpolation.

Water transparency was measured with a Secchi disk twice a year, usually in June or August and in October, under sunny conditions and in presence of a smooth water surface. The mean Secchi depth (SD) was 4 ± 0.04 m and was used to assess the vertical attenuation coefficient of light (K_d). According to Koenings and Edmundson (1991), the suggested SD × K_d value for water of moderate transparency is 2.28, leading to an approximate K_d value for the Romaine-2 reservoir of 0.57 m^{-1}. As a result, 50% of the absorption of incident solar radiation took place in the first 1.2 m of the water column, while the aphotic zone, defined as the region where solar radiation penetration is only 1% or less, began at a depth of 8.1 m.

The following thermal phases were identified and characterized in terms of duration and timing: the vernal and fall turnovers, the reverse winter stratification, and the summer stratification. Summer stratification was divided into two subperiods, that is the epilimnion growth phases from 0 to 15 m and from 15 m to the start of the fall turnover period. Phase identification was performed using the mean daily temperature profile. For example, the onset of mixing periods (i.e., vernal and fall turnovers) coincided with the homogenization of the temperature from top to bottom, while the onsets of summer and reverse stratifications were detected by slope changes in the vertical water temperature profile.

(ii) Heat storage

The heat storage flux is defined by

$$\Delta H_S = \int_0^H \rho_w c_{pw} \frac{\overline{\Delta T_w}}{\Delta t}\, dh, \tag{4}$$

where ρ_w is the water density (kg m^{-3}), c_{pw} is the specific heat of water (J kg^{-1} K^{-1}), ΔT_w is the water temperature

Brought to you by I.N.R.S. | Unauthenticated | Downloaded 03/14/24 01:14 PM UTC

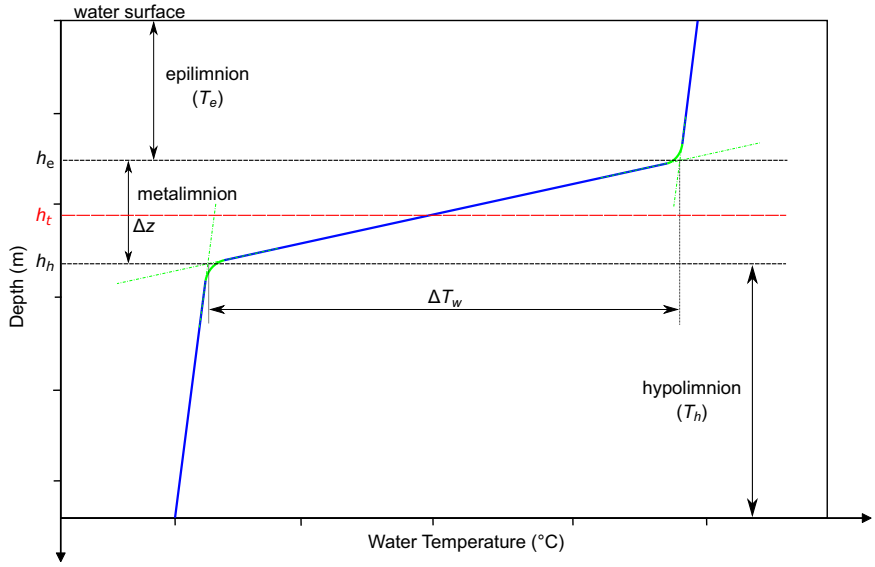

FIG. 2. Schematic of a vertically stratified temperature profile (blue line) showing the thermocline (red line) depth h_t (m), the metalimnion thickness $\Delta z = h_h - h_e$ (m), and the temperature amplitude ΔT_w (°C), as well as the epilimnion and hypolimnion zones. The term h_e is defined as the depth of the intersection between the temperature lines of the epilimnion and the metalimnion, and h_h is defined as the depth of the intersection between the metalimnion and hypolimnion. The green arcs represent the radii of curvature delineating the beginning and end of the metalimnion.

difference (K) between two time steps over a certain depth H (m), and Δt is the time step (here, 30 min). We considered H to be 70 m because no water temperature measurement was taken below this depth.

(iii) Thermocline characteristics

A key feature of a reservoir's thermal regime is the position of its thermocline. The metalimnion, the classic thermocline of Birge (1897), corresponds to a range of depths where a rapid decline in temperature occurs. It separates two regions of nearly homogeneous temperatures, the epilimnion (T_e) and hypolimnion (T_h), respectively. Hence the metalimnion is bounded by upper (h_e) and lower (h_h) depths and has a thickness defined by $\Delta z = h_h - h_e$, a temperature amplitude (ΔT_w) and a mean temperature gradient ($\Delta T_w/\Delta z$) (see Fig. 2). The thermocline lies within this zone and is defined as the water depth h_t (m) at which the maximum change in temperature occurs. Its temperature is T_t. The transition depths h_e and h_h are characterized by radii of curvature that indicate the transition from one layer to another. A simple algorithm was implemented to determine h_e and h_h. We iteratively compared the mean temperature of progressively thicker layers (from the surface/bottom) with the temperature of the next sensor until we encountered a difference greater than 0.5 K, at which point the depth was identified as either the beginning or the end of the metalimnion. Moreover, if the temperature amplitude ΔT_w was less than 1 K, we considered that there is no thermocline. Finally, h_t and T_t were calculated as the mean of h_e and h_h, and T_e and T_h, respectively, assuming that the temperature gradient was constant across the thickness of the metalimnion. The uncertainty associated with h_e, h_h, and h_t was estimated to be ±2 m.

4) HEAT BUDGET

The rate of change of the internal heat storage ΔH_S [Eq. (5) and Fig. 3a] of the water column within a hydropower reservoir depends on incoming and outgoing heat fluxes as follows:

$$\Delta H_S = (R_n + H_{\mathrm{adv},n}) - (H + \mathrm{LE}), \tag{5}$$

where R_n is the net radiation [Eq. (3)]; $H_{\mathrm{adv},n}$ is the net advection of heat [see Eq. (6)]; and H and LE are the sensible and latent heat fluxes, respectively [see section 2b(1)]. All terms in Eq. (6) are in watts per square meter (W m^{-2}). We calculated the annual (section 3c) and monthly (section 3d) heat budgets.

The net flux of advected thermal energy is written as follows:

$$H_{\mathrm{adv},n} = H_i - H_o = (H_{i_{\mathrm{up}}} + H_{i_{\mathrm{lat}}} + H_P) - H_o, \tag{6}$$

where H_i is the total energy input to the Romaine-2 reservoir, $H_{i_{\mathrm{up}}}$ is the input of energy from the upstream Romaine-3 reservoir, $H_{i_{\mathrm{lat}}}$ is the energy input from reservoir hillslopes and tributaries (e.g., natural runoff), H_P is the energy brought by precipitation, and H_o is the total energy output through water release of the Romaine-2 reservoir (all terms are in W m^{-2}). They represent, along with the turbulent heat fluxes, the most challenging heat budget terms to estimate. For deep reservoirs,

Brought to you by I.N.R.S. | Unauthenticated | Downloaded 03/14/24 01:14 PM UTC

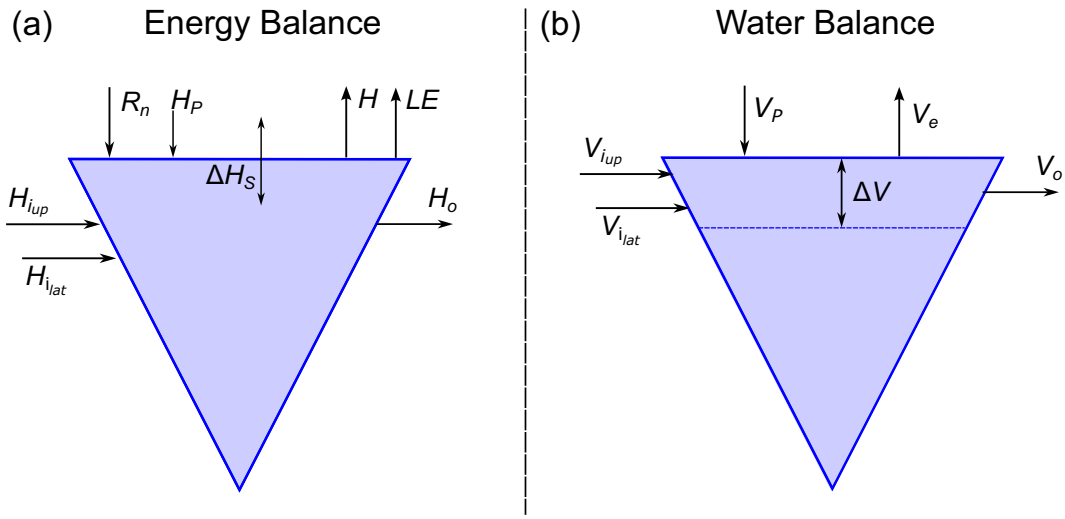

FIG. 3. Schematic of (a) the water balance, where V_P is the precipitation, V_e is the volume of evaporation, ΔV is the internal volume change, $V_{i_{\mathrm{up}}}$ is the input water volume from the reservoir upstream, $V_{i_{\mathrm{lat}}}$ is the input volume from lateral hillslopes, and V_o is the output volume; and (b) the energy balance, where R_n is the net radiation, H is the sensible heat flux, LE is the latent heat flux, ΔH_S is the heat storage, $H_{i_{\mathrm{lat}}}$ is the energy from reservoir hillslope, $H_{i_{\mathrm{up}}}$ is the energy from upstream Romaine-3 reservoir, H_o is the energy output for Romaine-2 reservoir operations, and H_P is the energy from precipitation (all terms are in W m^{-2}). The sign convention used here is the following: fluxes are positive (negative) when they come toward (away) from the water surface.

the water temperature at the bottom (T_h) can be assumed constant. The morphology of the reservoir (with a 22 km^{-1} surface to volume ratio) allows us to neglect energy exchanges at the reservoir sidewalls (i.e., reservoir–groundwater interface) and the underlying sediments (Hutchinson and Edmondson 1957), contrary to shallow water bodies (Momii and Ito 2008; Rouse et al. 2005).

The heat budget [Eq. (5)] highlights the dominant heat transfer mechanisms within the reservoir. Note that the energy state of a system is determined by its absolute temperature (Kelvin). In addition, as an open system, the Romaine-2 reservoir's sources and outputs must be considered, which implies a temperature difference in the net advection term. The advected heat fluxes H_x (W m^{-2}) in Eq. (6) were calculated following Xing et al. (2012) and Olsson et al. (2022):

$$H_x = \frac{\rho_w c_{pw} Q_x T_x}{A_0}, \tag{7}$$

where x can be any of the following: upstream inflow (i_{up}), outflow (o), lateral inflow (i_{lat}), or precipitation (P); ρ_w is the water density (kg m^{-3}); c_{pw} is the specific heat of water (J kg^{-1} K^{-1}); Q_x can be any one of the following flows: $Q_{i_{\mathrm{up}}}$, Q_o, $Q_{i_{\mathrm{lat}}}$, or Q_P (m^3 s^{-1}); T_x can be any one of the following temperatures: $T_{i_{\mathrm{up}}}$, T_o, $T_{i_{\mathrm{lat}}}$, or T_P (K); and A_0 is the maximum surface area of the reservoir (m^2). We estimated the precipitation temperature was the same as the air temperature. Daily water temperatures $T_{i_{\mathrm{up}}}$ and T_o, used to calculate $H_{i_{\mathrm{up}}}$ and H_o, were measured using temperature sensors (Apogee SDI Instruments) inserted in the scroll case upstream of the turbines. Note that for 2019/20, the turbine water temperatures were not measured correctly (see Fig. SM 2 in the online supplemental material). They were thus obtained as the mean value of the other years. The Q_P was calculated from precipitation measurements described in the water budget section (section 2c). Finally, tributary water temperatures $T_{i_{\mathrm{lat}}}$ were estimated using the empirical relationship developed by Harvey et al. (2011) for Newfoundland rivers, that is, for watersheds, latitudes, and climatic conditions similar to the present study:

$$T_{i_{\mathrm{lat}}} = \frac{\alpha}{1 + \exp[\gamma(\beta - T_a)]}, \tag{8}$$

where $T_{i_{\mathrm{lat}}}$ is the daily water temperature (K); α, β, and γ are coefficients averaged for the rivers considered by Harvey et al. (2011), yielding values of 19.01, 9.86, and 0.174, respectively; and T_a is the daily air temperature (K). We used 30-min data to better describe the daily air temperature, as the extrema may not represent the average pattern of water temperature. We tested this model with water temperature observations from the Bernard River, a tributary of the Romaine-2 reservoir, between 16 June and 8 October 2021. The coefficient of determination for the period under study was 0.74 and the bias was 0.05 K; performances deemed acceptable for our study. The temperature of precipitation T_P was assumed equal to the air temperature.

A thermal year from 1 March to 28 February was used to calculate heat budgets, as it was at this time of the year where the cumulative change in heat storage approached zero. Three thermal years were used in this study: 2019/20, 2020/21, and 2021/22. Note that, the reservoir water level was slightly different between the beginning and the end of each thermal year. Additional or reduced volumes were accounted for in

Brought to you by I.N.R.S. | Unauthenticated | Downloaded 03/14/24 01:14 PM UTC

TABLE 1. Internal volume and heat storage changes for each thermal year of the study period. The Δh and ΔV values represent the difference between the last day and the first day of the periods under consideration.

Thermal year	2019/20	2020/21	2021/22
Δh (m)	1.7	9.0	−4.3
ΔV (km^3)	0.14	0.71	−0.34
$H_{\Delta V}$ (MJ m^{-2})	2438	10 332	−4816

the heat budget calculations, to ensure budget closure. The temperature chosen for these volumes was that of the lateral inflow. Table 1 presents ΔV and the corresponding heat storage term for each thermal year.

Logistical constraints imposed by the remote location of the site prevented continuous measurements of ice and snow temperatures and thicknesses. However, a rough estimate of the energy required to melt them during spring, H_c (W m^{-2}), can be made. We estimated maximum ice and snow thicknesses of 85 and 20 cm, respectively, based on ice and snow sample cores taken during the 2021/22 winter. We assumed relative ice and snow densities of 0.92 and 0.3, respectively, and temperatures of −1° and −7°C for maximum cold content. These temperature values were chosen based on field measurements in the forest canopy snowpack near the reservoir. Also, these values were realistic for snow in this environment (DeWalle and Rango 2008; Seibert et al. 2021) and with Parajuli et al. (2021) that assessed the cold content of snowpack in a humid boreal forest. The energy H_c was then calculated using

$$H_c = m_i[c_{pi}(273.15 - T_i) + \lambda_{fi}] + m_s[c_{pi}(273.15 - T_s) + \lambda_{fi}], \quad (9)$$

where m_i and m_s (kg m^{-2}) are the masses of ice and snow, respectively; c_{pi} (J kg^{-1} K^{-1}) is the specific heat of ice and snow; T_i and T_s (K) are the temperatures of ice and snow, respectively; and λ_{fi} (J kg^{-1}) is the latent heat of fusion of ice. Using the equations and values presented above, we found $H_c = 283$ MJ m^{-2}. We assumed that the energy employed to melt the ice and snow cover was then no longer available for the heat balance of the Romaine-2 reservoir. In doing so, we reduced net radiation by H_c at the annual scale, assuming that the melting of the snow and ice cover was entirely due to incident solar radiation. To quantify the energy balance closure, we calculated the energy balance ratio (EBR) [Eq. (10)]. The H_c was subtracted from R_n when calculating the annual value:

$$\mathrm{EBR} = \frac{H + \mathrm{LE}}{(R_n - H_c) + H_{\mathrm{adv},n} - \Delta H_S}. \quad (10)$$

c. Water budget

The annual water balance (Fig. 3b) of the reservoir can be defined as follows:

$$\Delta V = (V_{i_{\mathrm{up}}} + V_{i_{\mathrm{lat}}} + V_P) - (V_o + V_e), \quad (11)$$

where all terms are in cubic meters (m^3); for the period under study, ΔV is the internal change in the stored volume, $V_{i_{\mathrm{up}}}$ and V_o are the upstream (entering) and downstream (exiting) volumes, V_P is the precipitation volume, V_e is the volume of evaporated water, and $V_{i_{\mathrm{lat}}}$ is the lateral (entering) volume from reservoir hillslopes and tributaries. Note that V_e is related to the latent heat flux LE through

$$V_e = \frac{\mathrm{LE}}{\lambda_v \rho_w}\Delta t, \quad (12)$$

where λ_v is the latent heat of vaporization (J kg^{-1}), ρ_w is the density of water (kg m^{-3}), and Δt is the period over which the evaporated volume was computed. Lateral volumes were linked to corresponding flows through

$$V_x = Q_x \times \Delta t, \quad (13)$$

where V_x refers to a volume (V_o or $V_{i_{\mathrm{up}}}$) and Q_x refers to a flow (Q_o or $Q_{i_{\mathrm{up}}}$), and x can be upstream inflow (i_{up}) or outflow (o), and Δt is the period of interest. The heat balance residual term reflects uncertainties in the observed energy fluxes, but also results from uncertainties in the water balance as shown in Eq. (11) (inflows and outflow involved in calculating energy fluxes).

Liquid precipitation was measured directly at the shore site using a TB4 tipping-bucket (Hyquest Solutions, United States), while solid precipitation was collected at the nearest Environment and Climate Change Canada weather station (Havre-Saint-Pierre), some 80 km south of the reservoir. From 1 November to 30 April, precipitation data from the Havre-Saint-Pierre station were used, while from 1 May to 30 October, corresponding to the period when air temperatures were above 0°C, data were taken from the shore station. Daily values for $V_{i_{\mathrm{up}}}$ and V_o were inferred from the power generated by the turbines, knowing their efficiency. The equation used here connects flow Q to turbine power P and efficiency η:

$$P = \eta \rho g Q \Delta h, \quad (14)$$

where P (W) is the turbine power, η is its efficiency (dimensionless), ρ is the water density (kg m^{-3}), g is the gravitational constant (9.81 m s^{-2}), Q is the incoming (Romaine-3) or outgoing (Romaine-2) flow (m^3 s^{-1}), and Δh (m) is the difference in height between the water intake and the downstream discharge.

Daily ΔV was obtained by multiplying daily reservoir area, taking from the storage curve, by the daily water level change Δh that was measured with a constant flow bubble gauge (Sutron Accubar dual orifice, Virginia, United States). Finally, the natural tributary inflow volume ($V_{i_{\mathrm{lat}}}$) remains challenging to assess accurately and, therefore, is typically assumed as the residual term of the water balance as it was done in this study.

3. Results and discussion

a. Hydropower and meteorological conditions

Figure 4 shows a subset of the meteorological variables recorded at the southern edge of the Romaine-2 reservoir. Summers were more humid but less windy than winters [wind

Brought to you by I.N.R.S. | Unauthenticated | Downloaded 03/14/24 01:14 PM UTC

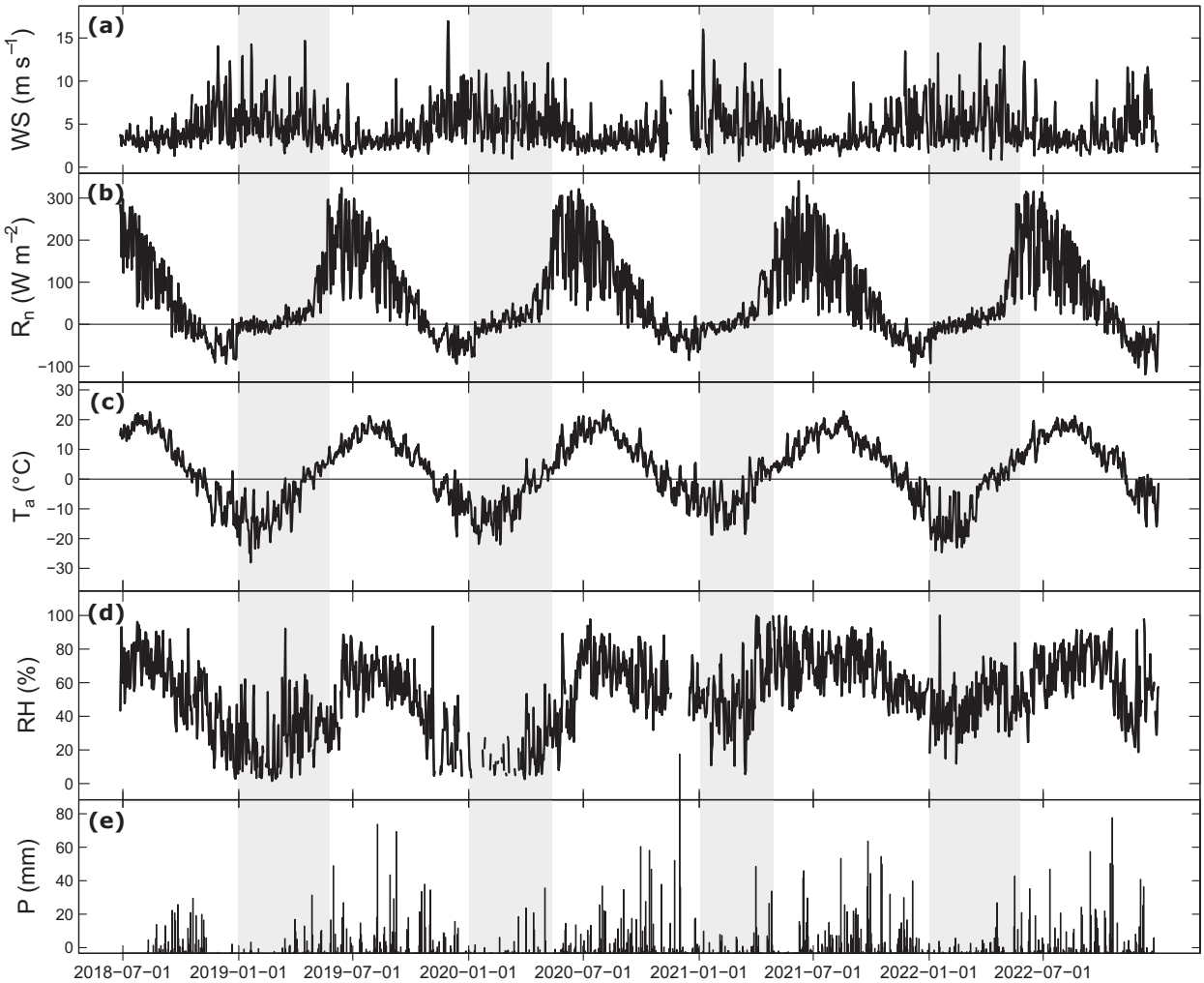

FIG. 4. Daily means of (a) WS, (b) R_n, (c) T_a, (d) RH collected at the raft and shore sites, and (e) P observed at the shore station and recorded at the nearest weather station. Shaded areas indicate the ice cover periods, which were identified using time-lapse photos of the southern end of the reservoir surface.

speed (WS) up to 15 m s^{-1}]. Mean daily net radiation peaked in June at about 300 W m^{-2} and reached a minimum of −80 W m^{-2} in December. Ice breakup occurred during a period of rapidly increasing radiation, which greatly accelerated thawing. Precipitation varied slightly from year to year (1008, 1153, 1339, and 1151 mm in 2019, 2020, 2021, and 2022, respectively).

b. Water budget

Throughout the study period (2018–22), hydropower generation involved large water level drops, up to 17 m in winter and 2 m during the ice-free period (Fig. 5a), resulting in a smaller surface area during these seasons. Romaine-2 and Romaine-3 reservoirs turbine flow rates also fluctuated throughout the year, with peaks in winter when energy demand was high and during the freshet to avoid spillage (Figs. 5b,c). During the ice-free period (May–December), the mean turbine flow rate out of the Romaine-2 reservoir was 220 m^3 s^{-1}, while the mean flow rate out of Romaine-3 (and into Romaine-2) was only 140 m^3 s^{-1}, hence the gradual decline in the Romaine-2 water level during that period. The spillway flow is not represented in Fig. 5 as it remained close to zero most of the year except in spring when it was used to release excess spring freshet water.

In general, the water level variation in the reservoir was cyclical, that is, the maximum level of 100 m was reached in mid-June, followed by slight fluctuations around 98 m until the end of December; then, a significant decline of 3 m per month occurred from January to mid-April, leading to an average minimum level of 89 m. The average hydraulic residence time is 5.4 months ± 10 days, and was obtained by dividing the average reservoir volume over a year by the total outflow volume over the same period. Note that this annual cycle varied from one year to another. From July to November 2020, the water level of the Romaine-2 reservoir dropped sharply by about 10 m due to the impoundment of the upstream

Brought to you by I.N.R.S. | Unauthenticated | Downloaded 03/14/24 01:14 PM UTC

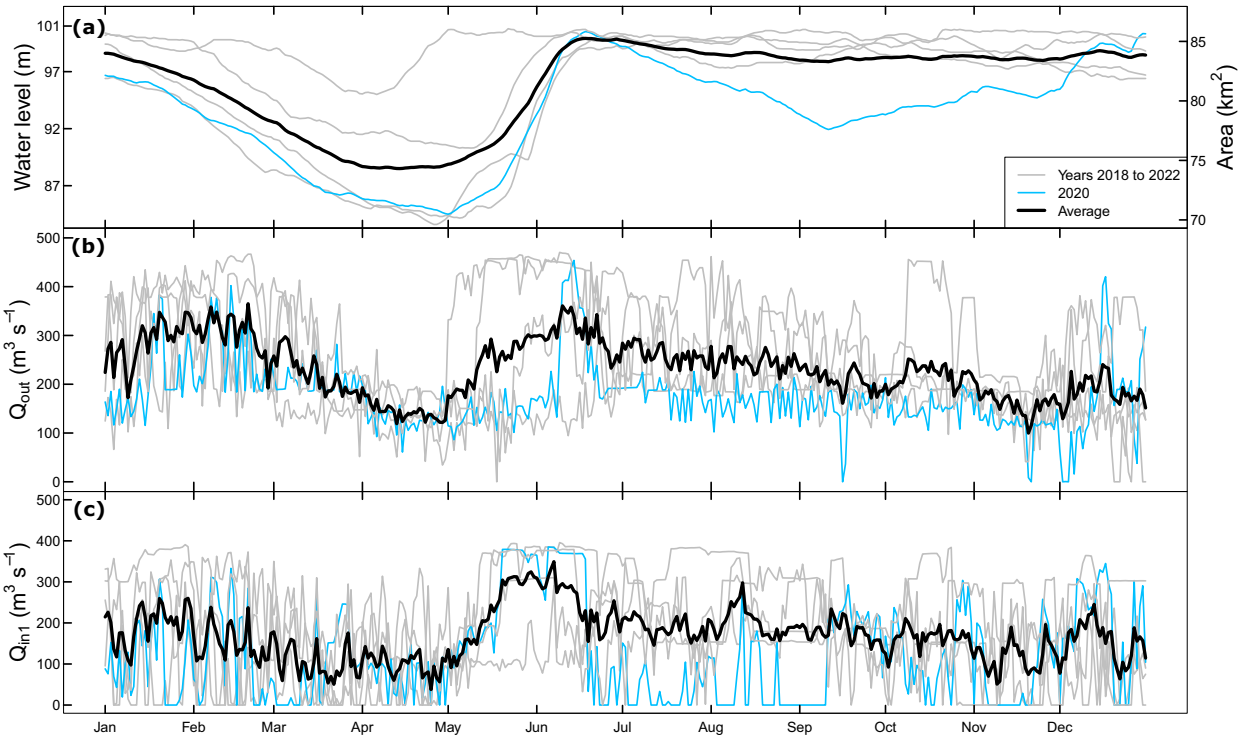

FIG. 5. Romaine-2 daily (a) water levels and (b) turbine outflow rate Q_o (m^3 s^{-1}), and (c) Romaine-3 reservoir turbine flow rate $Q_{i_{up}}$ (m^3 s^{-1}). The three plots show the mean (black solid line) and the observed values (gray lines) for years 2018–22. The year 2020 is displayed in blue as it was a specific year in terms of water management.

Romaine-4 reservoir. This affected the Romaine-2 thermal regime, as discussed in section 3e. Figure 6 shows the monthly water balance of the Romaine-2 reservoir.

The largest water budget fluxes occurred in May and June, as much of the upstream and lateral inflow took place during the spring freshet. The $V_{i_{up}}$ and $V_{i_{lat}}$ peaked at 1350 hm^3 month^{-1} in June and 500 hm^3 month^{-1} in May, respectively, coinciding with ΔV rising substantially at a rate of 6 m month^{-1}. The V_o evolved synchronously with $V_{i_{up}}$ so that the reservoir water level equilibrated and peaked at 1350 hm^3 month^{-1} in June during the vernal turnover, allowing efficient mixing of the water column. From July to December, the reservoir was recharged by significant lateral inflows, which forced V_o to be greater than $V_{i_{up}}$ to keep the reservoir level below the upper limit. Note that water was released through the spillway mainly in late May and early June, during the peak freshet. Interannual variability is due to fluctuations in turbine flow and the requirement to maintain water levels below the freeboard limit so that high water levels do not compromise the physical integrity of the reservoir.

On an annual basis, upstream and downstream flows were the main drivers of water movement within the reservoir. The outflow mainly consisted of turbine flow (~91.5%), while spilled flow contributed less than 8%. The same can be said for the water inflows, which were mostly turbine flow from the upstream Romaine-3 reservoir (69.5%), with spill and lateral inflow accounting for 10% and 20%, respectively. Direct precipitation and evaporation had a much smaller impact, with precipitation accounting for only 1% of inflows and evaporation amounting to only 0.5% of outflows. Evaporation and precipitation were two orders of magnitude smaller than the other terms, which was expected given the large volume of water passing through the turbines. Nevertheless, it is noteworthy that due to evaporation, less water was available for use downstream of the reservoir, including for power generation. If we compare the mean annual evaporative volume (50 hm^3) with the mean annual turbine volume (≈8200 hm^3), the corresponding power loss represented almost two days of turbine operation.

c. *Annual heat budget*

Figure 7 shows the annual heat budget of the Romaine-2 reservoir for the three thermal years of this study period (2019/20, 2020/21, 2021/22). The H_c [Eq. (10)], the energy required to melt the snow and ice cover (estimated at 283 MJ m^{-2}), was subtracted from the net radiation. We assumed that this value was approximately the same for each year, which obviously introduced some uncertainty. Depending on the year, H_c accounted for between 14% and 15% of the net radiation.

For these three thermal years, net radiation accounted for the majority of the total energy input, ranging from 62.2% to 79.1%, while the net advection of heat ($H_{\mathrm{adv},n}$) ranged from 16.2% to 37.5%. Regarding the outgoing terms, the latent heat flux amounted to 43.7% to 51.2% and represented about 3 times the energy released by the sensible heat flux, which ranged from 12.5% to 20.1%. The rate of change of heat storage, ΔH_S, was either a small source or sink term depending

Brought to you by I.N.R.S. | Unauthenticated | Downloaded 03/14/24 01:14 PM UTC

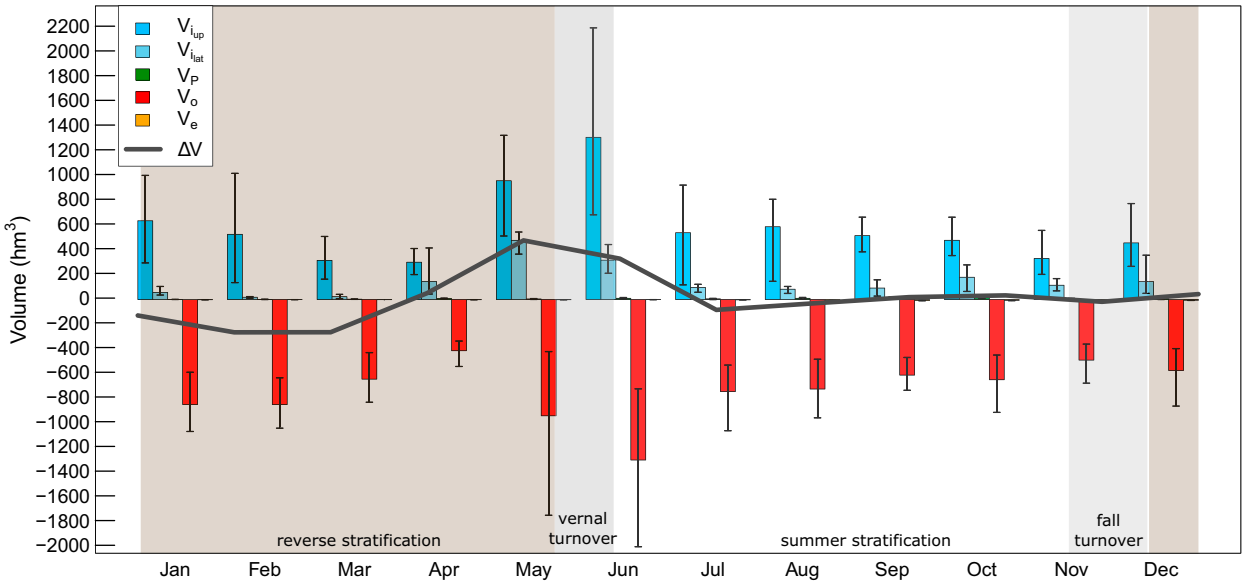

FIG. 6. Mean monthly volumes of the water budget for the Romaine-2 reservoir from June 2018 to December 2022. The term $V_{i_{lat}}$ is the lateral inflow and taken as the residual of the water balance, ΔV is the internal change of Romaine-2 volume, and $V_{i_{up}}$ and V_o are the upstream inflow and outflow, respectively. Both $V_{i_{up}}$ (i.e., from Romaine-3) and V_o are calculated from the sum of the turbine and spilled flows. The V_P is the daily volume of precipitation. Background colors refer to mean thermal phases (see section 3e). The lines indicate the minimum and maximum values.

on its sign due to its imbalance on these periods. Finally, the heat budgets exhibited a nonclosure term in the form of output energy, the residual, varying from 26.3% to 39.4%, which represented a significant value, indicating the presence of uncertainties on some of the terms. In other words, we measured more incoming energy into the reservoir than outgoing energy for each year of the whole study period.

Meanwhile, it has been shown that the eddy-covariance approach does not close the energy balance (Foken 2008) when solely measuring the turbulent heat fluxes. Based on the energy balance ratio introduced in Eq. (10), we obtained annual EBR values ranging from 0.6 to 0.72. Consequently, we can close the heat budget by adjusting the turbulent heat fluxes by preserving the Bowen ratio (Mauder et al. 2018), so that the residual term is nullified. When doing so, the contribution of LE is revised to 72.1%, 80.4%, and 67%, and H to 27.9%, 19.6%, and 28% for years 2019/20, 2020/21, and 2021/22, respectively. Now, if we refer to these values, more than two thirds of the incoming energy was released to the atmosphere in the form of latent heat flux, which remained the dominant way of dissipating heat, and less than 30% was lost through sensible heat. A similar result was obtained by Xing et al. (2012), who reported that latent heat flux accounted for 83% of the net radiation on the Kranji tropical reservoir (Singapore). Moreover, Rouse et al. (2005) showed that latent and sensible heat fluxes accounted for 80% and 20% of the net radiation for medium and large boreal lakes, respectively. For Great Slave Lake in northwestern Canada, Blanken et al. (2000) reported that latent and sensible heat fluxes varied between 50% and 75% and between 5% and 15% of net radiation from August to September. In Japan, Momii and Ito (2008) found that the latent flux accounted for 90% of the net radiation, while the sensible flux was about 10%. For the boreal Lake Mendota (United States), Ragotzkie (1978) showed that the latent heat flux was about 80% of the net radiation, while the sensible heat flux was about 20%. Finally, it appears that in more northern regions, latent heat flux decreases and sensible heat flux increases relative to net radiation due to colder temperatures (Leppäranta et al. 2016). Xing et al. (2012) also showed that the advected heat fluxes could be an important component of the heat budget. They estimated the mean net advective heat fluxes to be −4 W m^2. In our study, the net advective heat flux, $H_{\mathrm{adv},n}$, was much higher and varied from 11 to 29 W m^{-2}. This emphasizes that the net advective heat flux varies from one reservoir to another, as it is primarily governed by climate and operating rules. It appears that on annual time scales, the net advected heat was a major source of energy to the reservoir and thus to the turbulent heat fluxes. Moreover, on smaller time scales, advective fluxes can also contribute substantially to surface temperature and thus indirectly to turbulent heat fluxes (Schmid and Read 2022).

d. *Monthly heat budget*

Figure 8 shows the monthly heat budgets. Contrary to the annual scale, we did not consider the energy used for ice melting at the monthly time step. Therefore, in May, the high residual (~180 MJ m^{-2}) was approximately equivalent to the amount of energy used for ice and snow cover melting. This value is not so far from the H_c value computed (283 MJ m^{-2}). We can clearly see that there was little energy exchange from January to April, when all terms were around 50 MJ m^{-2}.

Brought to you by I.N.R.S. | Unauthenticated | Downloaded 03/14/24 01:14 PM UTC

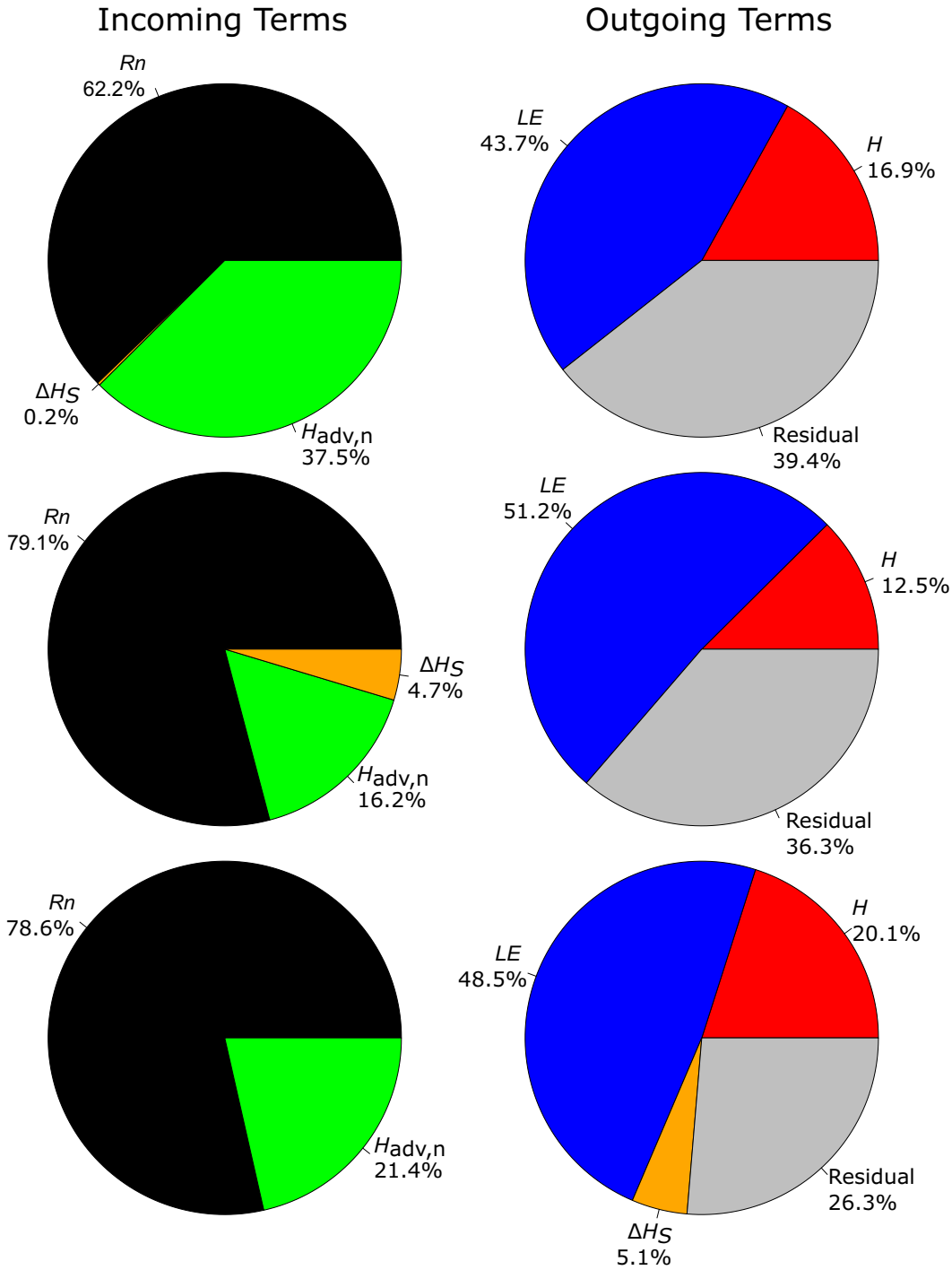

FIG. 7. Pie charts of the overall annual energy balance of the Romaine-2 reservoir from 1 Mar to 28 Feb for (top) 2019/20, (middle) 2020/21, and (bottom) 2021/22. The entering energy is in incoming terms, while the leaving energy refers to outgoing terms. The term R_n is the net radiation; $H_{\mathrm{adv},n}$ is the net advection of heat; H and LE are the sensible and latent heat fluxes, respectively; ΔH_S is the heat storage calculated over the top 70 m; and "Residual" refers to the missing energy reflecting the nonclosure. Note that H_c (fraction of net radiation energy used to melt the ice and snow cover) is removed from R_n.

Brought to you by I.N.R.S. | Unauthenticated | Downloaded 03/14/24 01:14 PM UTC

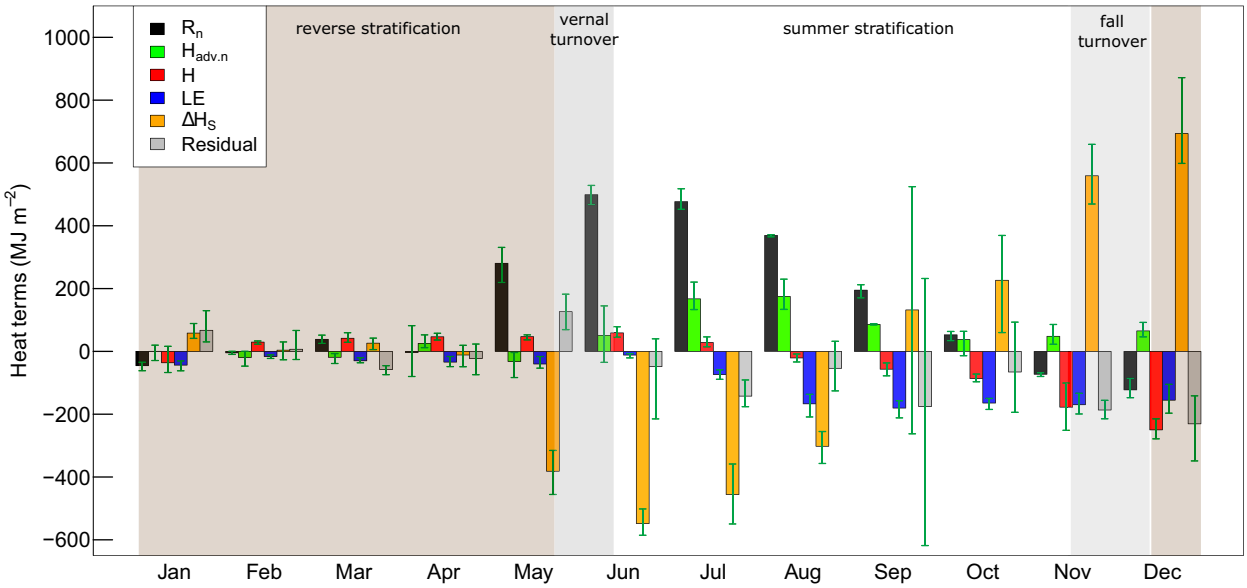

FIG. 8. Average monthly energy balance of the Romaine-2 reservoir for the 1 Mar 2019–28 Feb 2022 period. The entering terms (incoming) are positive while the leaving energy term (outgoing) are negative. The term R_n is the net radiation (black); $H_{\mathrm{adv},n}$ is the net advection of heat (green); H and LE (red and blue) are the sensible and latent heat flux, respectively; ΔH_S (orange) is the heat storage calculated over the top 70 m; and Residual (gray) refers to the missing energy reflecting the heat budget nonclosure. Note that, the radiative energy used for ice and snow cover, H_c, was subtracted from R_n. Green arrows represent the minimum and maximum for each term over the three years. Background colors refer to mean thermal phases (see section 3e). The sign convention used here is the following: fluxes are positive (negative) when they come toward (away) from the water surface.

This was due to the very low evaporative demand, the low net radiation, and the ice and snow cover that impeded the energy exchange between the reservoir and the atmosphere. Advective heat fluxes remained low as well because of the low water temperatures (below 4°C) entering and leaving the reservoir. However, from May to September, energy rapidly went into the reservoir mainly in the form of net radiation, and this energy was stored in the water column (negative ΔH_S, that is away from the water surface). The other major source of heat was through net advective fluxes, which were low from January to April, but in excess of 50 MJ m^{-2} the rest of the year. More precisely, $H_{\mathrm{adv},n}$ was sustained in July and August (200 MJ m^{-2}), while it remained positive and lower than 80 MJ m^{-2} from September to December. This positive $H_{\mathrm{adv},n}$ was explained by the higher $T_{i_{\mathrm{up}}}$ and $T_{i_{\mathrm{lat}}}$ from upstream and lateral inflows compared to outflows from June to August (see Fig. SM 5), and also by the higher volume of inflows than outflows.

As described in Pierre et al. (2023), the turbulent heat fluxes had the following pattern: H contributed to the reservoir heat (positive flux, i.e., toward the water surface) from February to July before increasingly releasing heat from August to January on average (negative flux, or away from the water surface). On the other hand, LE remained negative (away from the water surface) throughout the year, with small and persistent values from January to June and from July to December, respectively. Note that in December, the Bowen ratio (H/LE) reached 1.5, meaning that, at that time of the year, the main means by which the reservoir released heat to the atmosphere was through the sensible heat flux, due to the cold air above. Vernal turnover occurred when R_n was maximal, injecting large amounts of energy into the reservoir and homogenizing the temperature of the water column. Similarly, the fall turnover occurred when ΔH_S, H, and LE were sustained, returning heat stored in the reservoir back into the atmosphere.

Monthly heat content nonclosure was also determined, as a large residual was observed at certain times during the year: May (ice-off and vernal turnover), in July (high $H_{\mathrm{adv},n}$), in September (transition from heat stored and heat released), in November (fall turnover and sustained H and LE) and in December (sustained H and LE). Variability of the heat budget terms was moderate from year to year. In September and October, corresponding to the transition between the energy storage and release phases (ΔH_S changing sign), ΔH_S variability was great as it changed depending on the timing of that transition.

In 2020/21, the late summer 9-m drop in water level (see Fig. 5a) was responsible for variations in turbulent heat fluxes compared to other years. Namely, the sensible heat flux was 275 MJ m^{-2}, compared to a 430 MJ m^{-2} mean for 2019/20 and 2021/22. This lower H occurred simultaneously with lower water temperatures T_w during the open-free season. In 2020/21, the higher output advection flow, H_o, resulted in a drop in the water level of the reservoir, but more importantly in an increase in the energy extracted from the reservoir by turbines. As a result, the temperature of the reservoir's water column was reduced, as was its surface temperature. The substantial 9-m drop

Brought to you by I.N.R.S. | Unauthenticated | Downloaded 03/14/24 01:14 PM UTC

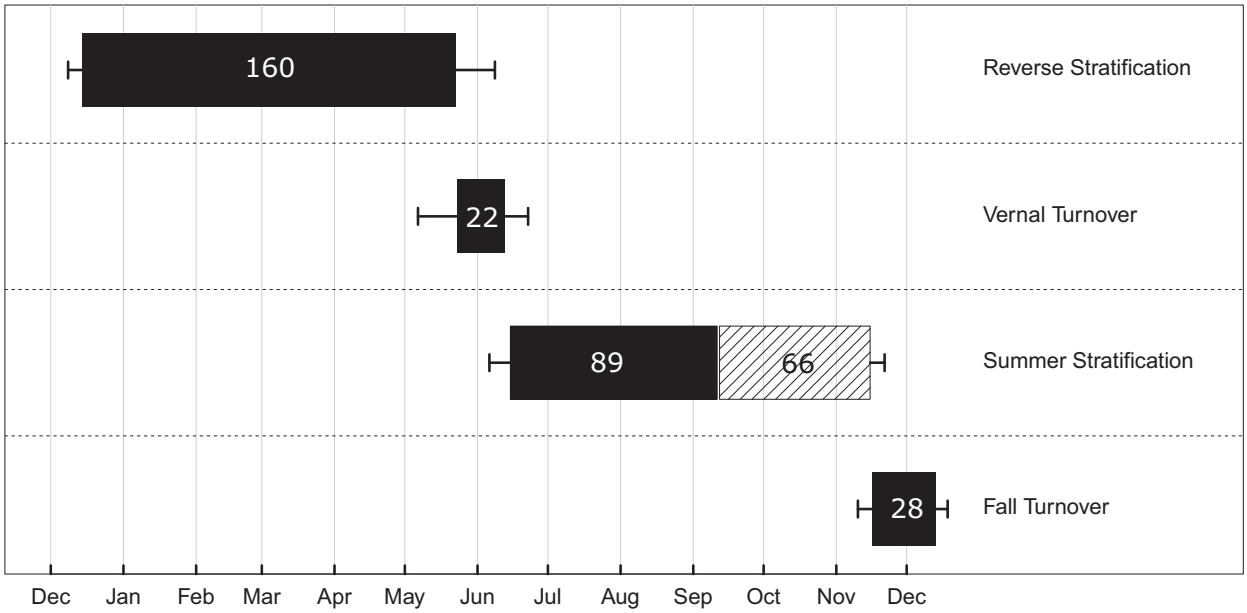

FIG. 9. Average length of each thermal phase of the Romaine-2 reservoir for the whole study period. Phases include vernal turnover, summer stratification, fall turnover, and reverse stratification. Numbers indicate the mean length (in days) of each thermal phase and bars indicate the standard deviations of start and end for each phase. Summer stratification is split in two phases: the epilimnion growth from surface to 15 m (black) and from 15 m to fall turnover (white hatched).

in 2020 had a dual impact as it (i) represented a significant loss of thermal energy (see Fig. 11 below) and water and (ii) led to conditions altering the thermal structure and energy fluxes of the reservoir.

e. *Thermal regime*

The heat fluxes presented in the previous section are highly dependent on mixing and stratification processes in the reservoir water column.

The fall turnover in November–December lasted on average 28 days, while the vernal turnover from mid-May to mid-June typically lasted 22 days (Fig. 9). The vernal turnover displayed more variability in the start and end dates than the fall turnover did. For example, in 2021 and 2019, vernal turnover started on 5 May and on 12 June, respectively, and ended on 7 June and on 27 June, respectively. The beginning of fall turnover occurred on 15 and 17 November, and the end took place on 7 and 14 December in 2021 and 2019, respectively. During the vernal turnover, the temperatures of the upper layers dropped to those of the deep layers (thermal homogenization). In spring, snowmelt runoff injected cold water into the reservoir, with temperatures below 4°C, which maintained the heat budget in a low state during several weeks before growing in mid-June. This cold water remained at the surface, on top of the warmer (and denser) water below, until it warmed up to 4°C and allowed vernal mixing to begin. On average, we observed a 31-day delay between ice-off and the start of the summer stratification.

On average, the reverse stratification lasted from mid-December to mid-May, for a total of 160 days (>5 months). The onset occurred between 5 and 21 December, while the end took place between 10 May and 15 June. The water temperature dropped to 1.5°, 2°, and 2.3°C at 20, 30, and 40 m deep, respectively, between March and the beginning of May (Fig. 10) while at depth it remained above 2.3°C. Hence, the minimum heat storage occurred at the beginning of March.

Summer stratification began on average in June (between 6 and 27), ended in mid-November (between 4 and 20), and lasted about 155 days (Fig. 9). It took 89 days for the epilimnion to grow from the surface (0 m) to a depth of 15 m between mid-June and mid-September, and 66 days for the epilimnion to grow from a depth of 15 m to about 40 m (roughly corresponding to the onset of fall turnover) between mid-September and mid-November. These two subperiods had a ±16 and ±18 days variation in length, respectively. Finally, we note that the top 1-m temperature peaked in mid-August, reaching 20°C or higher each year for about 10 days before starting to decline. We identified that the maximum amount of energy stored within the reservoir occurred around mid-September, about a month after the maximum temperature in the upper layers of the reservoir. In other words, the reservoir needed about 6.5 months to achieve its maximum energy state and about 5.5 months to return to its lowest level, which suggests that heat was removed from the reservoir slightly faster than it was stored. For comparison, Oswald and Rouse (2004) showed that the dimictic Great Slave Lake in the boreal region began to stratify in the second week of July with a thermocline formed at a depth of 9 m. However, due to its high latitude, the lake started to cool down mid-August instead of mid-September for the Romaine-2 reservoir, with low radiation and high wind helping to cool down the lake afterward.

Brought to you by I.N.R.S. | Unauthenticated | Downloaded 03/14/24 01:14 PM UTC

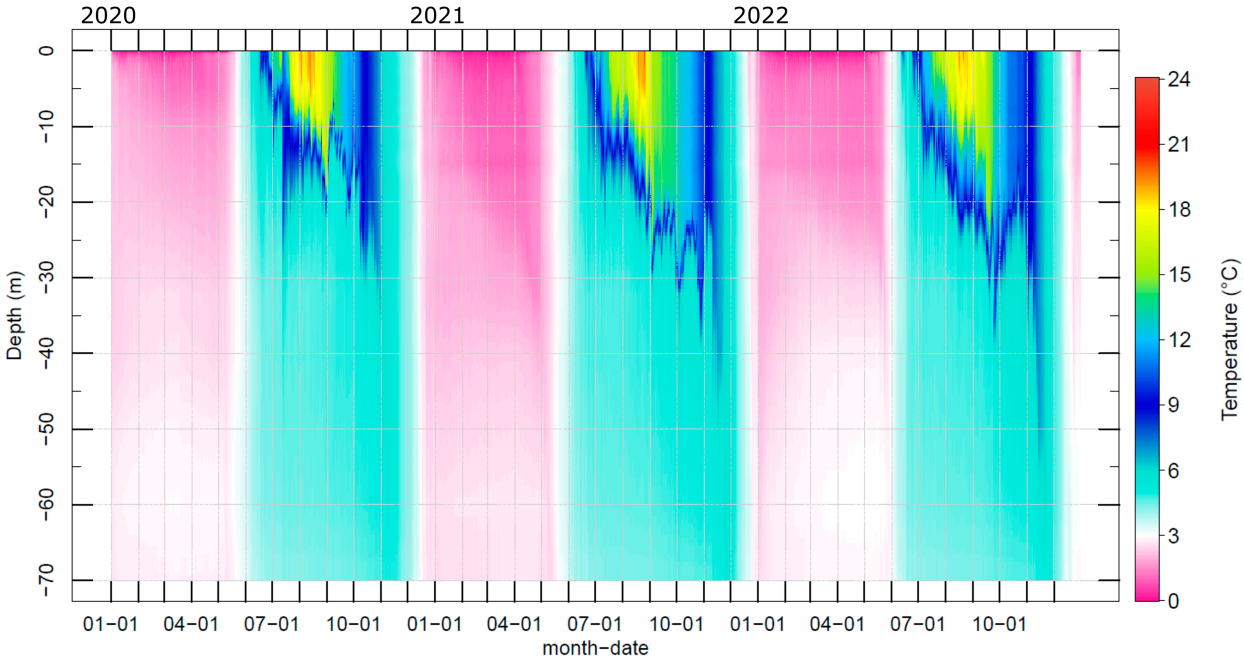

FIG. 10. The 30-min time series of temperature profiles from 1 Jan 2020 to 31 Dec 2022. Data beyond this period have gaps in time or in information from the thermistor chain.

The year 2020 represented a special case, with a cooler temperature profile than in 2021 and 2022 (Fig. 10). A maximum water temperature of 18°C was observed at 15 m in 2020, while it was recorded at 20 and 23 m in 2021 and 2022, respectively. Also, since the amount of heat stored was lower, the amount of heat to be dissipated was smaller and the fall turnover appeared 12 days sooner than in all the other years. This was directly attributable to the sharp decline in the reservoir level between July and November. Indeed, the high outflow resulted in a large amount of energy extracted from the Romaine-2 reservoir, which was not balanced by the low upstream inflow entering Romaine-2. Accordingly, it shows that the Romaine-2 reservoir management directly contributed to the thermal regime (Fig. 11).

The heat storage (Fig. 11) followed an annual cycle with a mean maximum of 1950 MJ m^{-2} in September and around 0 MJ m^{-2} in March. About 20% and 60% of the total heat storage was within the top 5 and 15 m, respectively. It also indicated that the deeper the water column, the stronger fluctuations in heat storage. Finally, the total amount of stored energy varied between years: in 2020, it reached a 1600 MJ m^{-2} while in 2021 it peaked at more than 2000 MJ m^{-2} over the 70-m water column, corresponding to a 20% difference. Moreover, in 2020, minimum storage coincided with a 10-m drop in the reservoir water level during the summer. Indeed, Romaine-2 turbine flow was lower than those of the other years and upstream inflow was very low with values closed to 0 m^3 s^{-1}. This confirmed that the hydrology imposed through reservoir management substantially affects heat storage and, thus, the thermal regime.

f. *Thermal structure and thermocline*

Changes in the thermal regime of a reservoir indirectly affect the timing of the heat budget and, in particular, the release of energy to the atmosphere through turbulent fluxes. Figure 12 presents the daily characteristics of the thermocline for the ice-free period from 2018 to 2022. In general, during the summer stratification, the epilimnion starts to grow from the surface of the top layer while the thermocline moves deeper at a steady rate of approximately 0.2 m day^{-1} from end of June until November. On average, from mid-June to mid-August (2 months), T_t rose from 6° to 12°C before declining until mid-November (3 months). The growth of the epilimnion is more irregular than the decline. The metalimnion temperature amplitude ΔT follows the same pattern with a maximum of 14°C in mid-August due to high surface water temperatures (approximately 20°C) and low subsurface temperatures (6°C). It then declines more steadily with a mean rate of approximately −1.3°C $week^{-1}$ before vanishing in November (fall turnover).

The h_t starts between 3 and 6 m on 20 June and increases steadily in open water, typically reaching 10 m in early July, 20 m in late August, 30 m in October, and 40 m in early November before the fall turnover. The temperature gradient $\Delta T_w/\Delta z_{\mathrm{meta}}$ evolved differently: it increases until September, when it stabilizes at a maximum value of approximately 0.8°C m^{-1} on average. Thereafter, the temperature gradient decayed at a mean rate of −0.15°C m^{-1} $week^{-1}$ until the onset of the fall mixing phase.

The summer thermocline lasts on average 155 days between 9 June and 10 November. Overall, the thermocline initially has a strong amplitude and a weak temperature gradient, then

Brought to you by I.N.R.S. | Unauthenticated | Downloaded 03/14/24 01:14 PM UTC

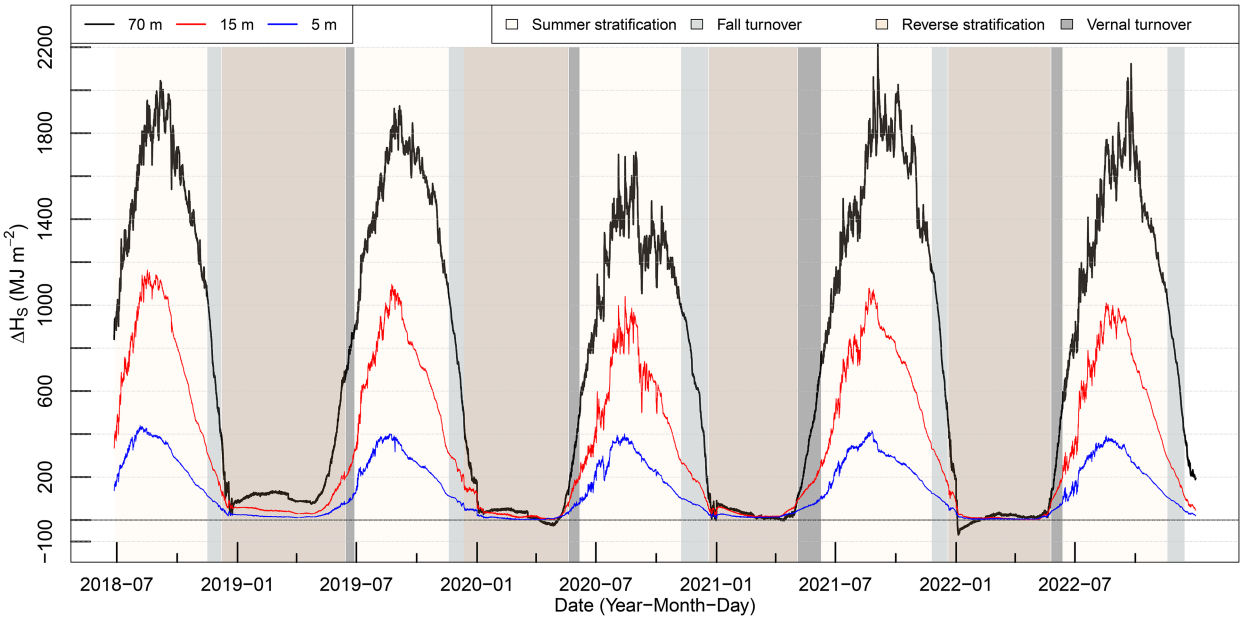

FIG. 11. The 30-min heat storage over the 70-, 15-, and 5-m-deep water column of the Romaine-2 reservoir for the entire study period. The reference point representing no storage (0 MJ m^{-2}) was chosen as the mean of the lowest heat storage between each year.

a weaker amplitude and a more intense temperature gradient. Similar results were found by Read et al. (2011), who showed that the metalimnion of Lake Mendota (43.1°N, 89.4°W; 39.4 km^2, maximum depth of 25 m) (Wisconsin) decreased in thickness between August and October. The thermal regime of the Romaine-2 reservoir is very comparable to that of water bodies at the same latitude and with the same climate (Bolsenga 1975; Nordbo et al. 2011; Vincent et al. 2008).

The lag between the maximum temperature amplitude (August) and the maximum temperature gradient (September) is about one month. Between these two dates, the metalimnion thickness decreases faster than the thermal amplitude, increasing the temperature gradient. From mid-September to November, the temperature gradient gradually declines, allowing wind mixing to take place and thus increasing the thickness of the epilimnion.

Once again, we confirm the connection between the water management regime and the thermal structure of the Romaine-2 reservoir. For example, in 2020, the 9-m decline in the water level, due to low outflow and almost no upstream flow, resulted in a 10-m rise in the thermocline, from −20 to −10 m, a colder thermocline temperature than for the other years, and a thermal gradient exceeding 1°C m^{-1} from the end of August to mid-September (Fig. 12). In November 2021, water level dropped by 2 m, resulting in a change of the thermocline from −22 to −35 to −20 m. This also caused an increase in the thermal gradient due to a stagnation of the temperature of the epilimnion over 8 days, from 8 to 16 October, and a decrease in the thickness of the metalimnion. Finally, mid-September 2022 (from 17 to 23), the outflow fluctuated between 150 and 250 m^3 s^{-1} and the thermal gradient rose when the metalimnion thickness decreased.

The thermal regime of this large hydropower reservoir varies significantly over the course of the year because of the downstream water release. Figures 5 and 10 offer an insight between the thermal structure and the outflow of the Romaine-2 reservoir. The main period of water level variation (associated with hydroelectric production) occurs between January and May, when the reservoir is either inversely and weakly stratified (January–April), or in a mixing period (April–May). From June to December, the reservoir is in a steady state in terms of water level, which remains relatively constant (lower water release). At this time, however, the thermal regime undergoes a major transformation (summer stratification) in intensity and depth. Finally, the great drop in water level in 2020 made the heat storage weaker, modified the thermocline depth, and preserved the thermal structure's integrity. Consequently, the influence of Romaine-2 reservoir operation on the thermal structure appears moderate.

4. Uncertainties

a. *Nonclosure problem of the energy budget*

The energy balance is affected by the problem of nonclosure due to the various uncertainties present throughout its calculation procedure. The main measurement errors are as follows. First, not all variables were measured directly. Indeed, some were derived from models or approximated by indirect methods. For example, the water temperature featured in the $H_{i_{lat}}$ lateral advection term was estimated using an empirical model solely based on air temperature. This introduced an inherent error that could have been reduced by directly measuring the average temperature of the tributaries using dedicated sensors. Also, turbine flow rates were inferred from

Brought to you by I.N.R.S. | Unauthenticated | Downloaded 03/14/24 01:14 PM UTC

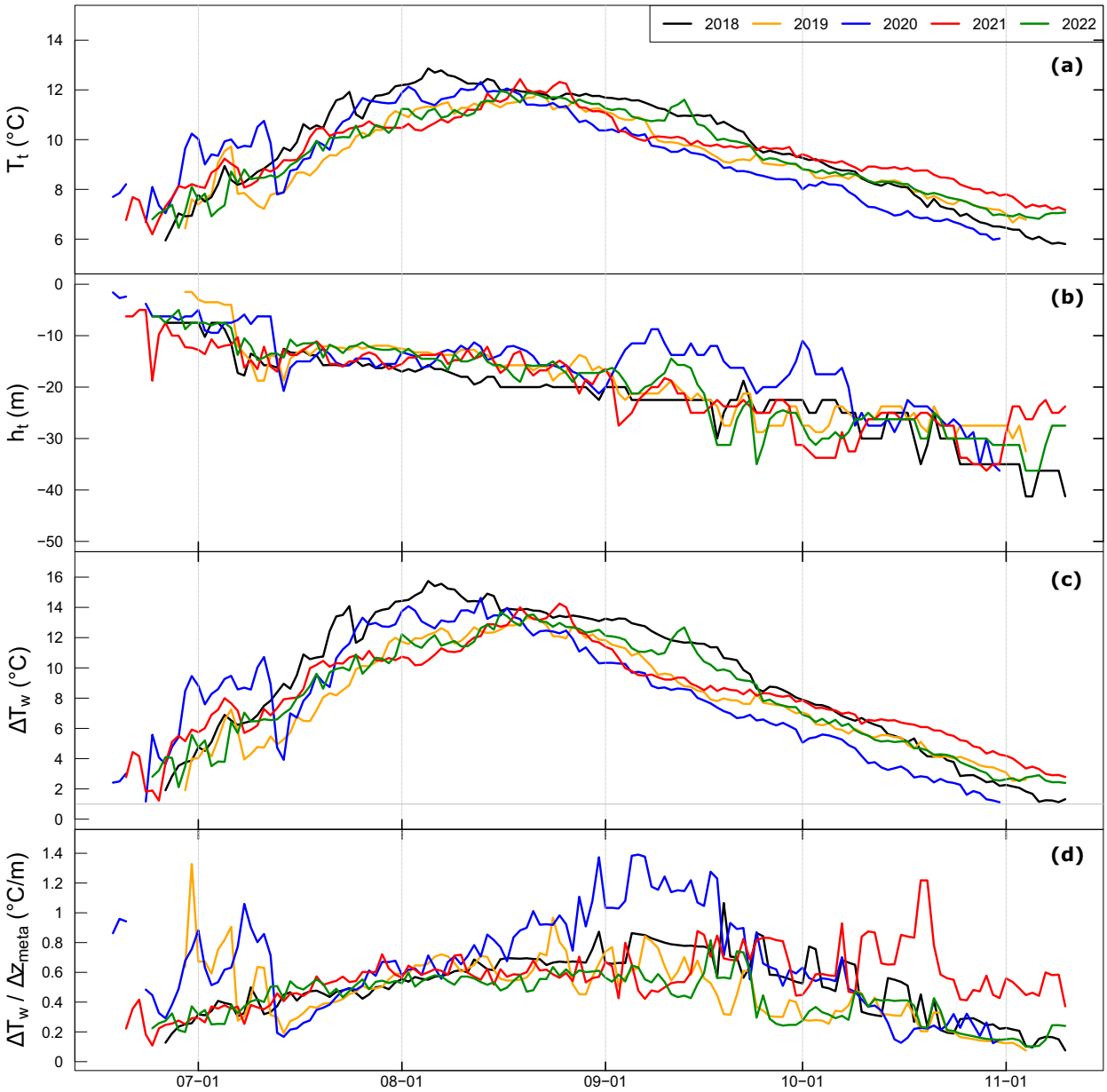

FIG. 12. Daily (a) thermocline temperature (T_t), (b) thermocline depth (h_t), (c) metalimnion temperature amplitude, and (d) metalimnion temperature gradient, for the ice-free period from 2018 to 2022.

power outputs, an indirect measure. Second, not all measurement scales were fully representative of the reservoir system (i.e., as a whole). A reservoir the size of Romaine-2 certainly has spatial variability in its energy and water balance due to its bathymetry, variable meteorological conditions over its extent (about 1.3 km × 65 km), inflows from surrounding streams, and so on. It would therefore be desirable to use larger-scale approaches to capture this spatial variability. For heat fluxes, one possible approach is to use microwave scintillometry, which can capture fluxes over a larger footprint than the eddy covariance approach (Bouin et al. 2012; Pierre et al. 2022). Remote sensing could also be used to measure surface temperature and infer fluxes over the entire reservoir. Finally, surface energy balance measurements on the water (from the raft station) were only made for the 4-month open water period each year. For the rest of the year, we had no choice but to use flux data measured from the shore. These data were often contaminated by edge effects (especially winds coming from the wrong direction) and had to be discarded and gap filled, adding to the uncertainty.

Thus, to establish an energy balance of a reservoir or lake, it is strongly recommended to, first, carry out in situ measurements of each of the terms at the appropriate scale, and then, for as long as possible, using the most appropriate measurement

Brought to you by I.N.R.S. | Unauthenticated | Downloaded 03/14/24 01:14 PM UTC

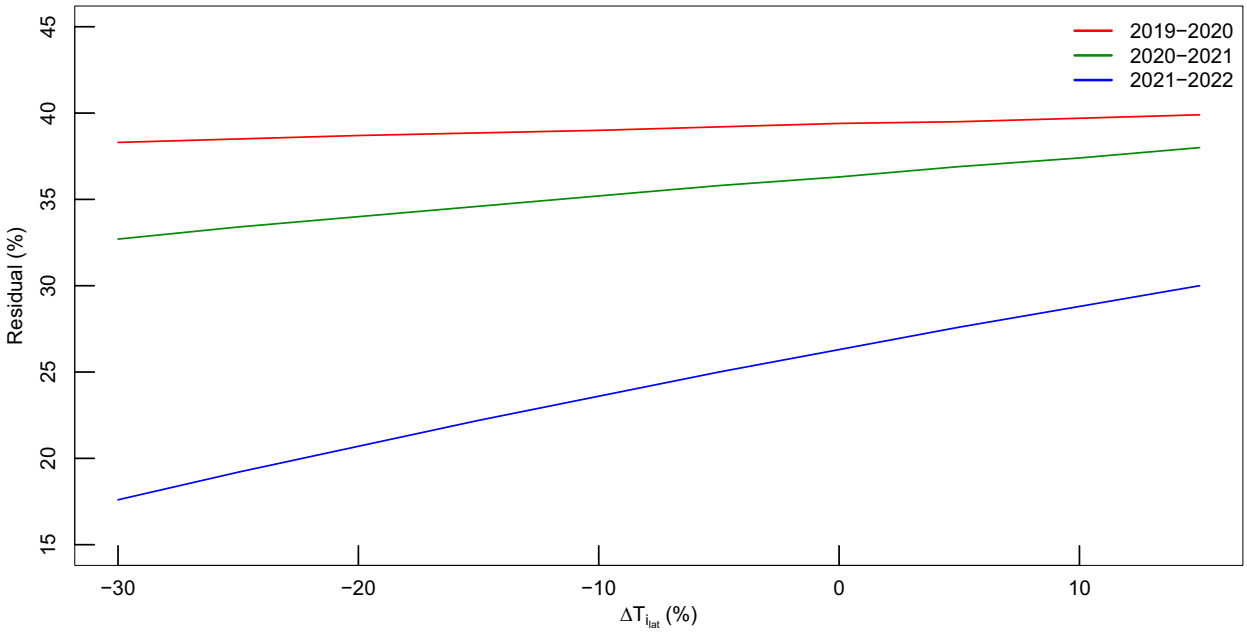

FIG. 13. Sensitivity analysis of the change in water temperature of lateral inflows $T_{i_{lat}}$. This graph displays the Residual term of the heat budget (%) as a function of the change in water temperature of lateral inflows, for the three thermal years.

method. This requires overcoming certain difficulties inherent to field work in a cold environment (presence of ice, etc.), which is not always feasible or even realistic. We detail two aspects of these shortcomings below, namely, the estimation of water temperatures and turbulent heat fluxes.

b. *Water temperatures*

The temperature of the lateral inflow is the only term of the energy budget for which we do not have direct measurement and could be therefore considered as one of the most uncertain. The $T_{i_{lat}}$ was estimated with the nonlinear model proposed by Harvey et al. (2011), which showed a good correlation (R^2 up to 0.74) with in situ observations of a small stream monitored over several months. We estimated the deviations from true values to be small, which was expected since the formula is representative of a northern boreal environment. Figure 13 shows the change in the residual term of the heat budget as a function of the temperature variation of the lateral inflow $\Delta T_{i_{lat}}$, for the three thermal years. We observed that the lower value of $\Delta T_{i_{lat}}$, the lower the residual, regardless of the year. Moreover, the greater the volume of lateral inflow, the greater the sensitivity of the residual term. By decreasing the temperature of the lateral inflow by 30%, LE represents 44.5%, 54%, and 54% of the outgoing energy (instead of 43.7%, 51.2%, and 48.5%), and H represents 17.2%, 13.4%, and 22% (instead of 16.9%, 12.5%, and 20.1%) for years 2019/20, 2020/21, and 2021/22, respectively.

Another source of uncertainty in the water temperature is due to the coarse resolution of the measurements performed in the reservoir water column. Measurements made beyond 10 m had a coarser resolution (one sensor every 2.5 m up to 32.5 m and every 10 m deeper), with an accuracy of 0.1°C. This means that beyond 10 m, each sensor was assumed to be representative of a 2.5-m-thick layer at best. A mischaracterization of the water temperature by 0.1°C over the 70-m-deep water column would lead to a difference of 0.029 MJ m^{-2}. We also assumed that the reservoir was constituted of several water layers homogeneous in temperature, which was not exactly the case. An intercomparison of the two thermistor chains separated by 1 km showed that the two temperature profiles deviated by less than 0.1°C from one another at most when considering monthly averages but can reach 2°C when looking at more frequent data.

While the temperature measurement of the water going through the turbines is less prone to error, the amount of water is harder to determine precisely. It cannot be measured directly, but only inferred from the power generated by the turbines, knowing the efficiency of each turbine. Moreover, the temperature of water exiting via the spillway was assumed to be the same as the deeper turbine water temperature whereas the former is from surface water. But this hypothesis is supported by the spilled water occurring mainly in May and June when the water column was homogeneous in temperature.

The processes involving heat exchange with water are also prone to uncertainty. For instance, the calculation of the net advection of heat was challenging since the Romaine-2 reservoir was not under a steady-state regime. To achieve a pseudo-steady-state regime, the excess energy corresponding to the additional volume was evaluated using the hypsometric curve and the temperature of the water going through the Romaine-2 turbines. The heat exchange between water and the banks was not considered in this study because it is difficult to quantify but is likely to have a minor influence in the energy budget as the reservoir is deep and compact.

Brought to you by I.N.R.S. | Unauthenticated | Downloaded 03/14/24 01:14 PM UTC

c. Turbulent heat fluxes

Eddy covariance is a state-of-the-art technique to estimate turbulent heat flux, but the measurements are nonetheless affected by several sources of uncertainty. The most important one is probably that the eddy-covariance method tends to underestimate turbulent heat fluxes as the technique may fail to capture exchanges for the smallest and largest eddies (Foken 2008). The literature reports that up to 35% of the energy imbalance can be attributed to this technical limitation, which approaches the annual residual term that varies between 26.3% and 39.4% in this study.

The motion of the raft contaminates the measurement of atmospheric turbulence, which was corrected using data collected from an accelerometer installed on the raft [section 2b(1)]. This added an extra step of data acquisition and flux calculation, and thus another source of uncertainty. These oscillations are also likely to affect radiation measurements, as it was not possible to keep the net radiometer in a stable position. This can then affect the net radiation estimates R_n. However, this uncertainty is expected to be small as the overall measurement should not be biased. Indeed, the radiometer oscillates with the raft about a horizontal position and deviations from this position should cancel out over sufficiently long periods.

Fluxes measured by the eddy-covariance towers may not be fully representative of the fluxes at reservoir scale, as the measurement footprint does not exceed 3% of the reservoir area. This implies that, without additional measurements, we must assume that the reservoir is spatially homogeneous over its extent, which it is assuredly not. This might have an effect on the magnitude of the turbulent fluxes and underlines the need to take measurements at broader scales with instruments such as scintillometers (Pierre et al. 2022). Random sampling uncertainty (Finkelstein and Sims 2001) is another source of error in this study, and it accounts for about 2% for sensible and latent heat fluxes. Finally, several algorithms were applied to filter out turbulent fluxes of lower quality (Pierre et al. 2022), resulting in gaps in the time series. These gaps were filled with a standard procedure (Reichstein et al. 2005), but despite a good performance, it introduces some uncertainty in the heat budget (Mahabbati et al. 2021).

5. Conclusions

In this study, we showed that the dam management operations performed at the Romaine-2, which is part of a cascading reservoir system located in the subarctic region, alter its thermal regime and thus its interactions with the atmosphere. We analyzed the thermal regime of a deep dimictic hydroelectric reservoir in eastern Canada from June 2018 to 2022. Thanks to this unique dataset built using two eddy-covariance installations, two thermistor chains, and inflow and outflow data provided by the operator of hydroelectric reservoir, we assessed the water and heat budgets at various time scales.

The reservoir water balance was dominated by the upstream inflow of the Romaine-3 reservoir and the outflow from the Romaine-2 reservoir. The input volume from the reservoir tributaries was estimated to be 20% of the total inflow, as a residual of the water budget. On the other hand, evaporation and precipitation were very small in volume. Spilled and turbine flow maxima occurred in spring due to the release of water from spring freshet. The hydraulic residence time was 5.4 months ± 10 days.

The annual heat budget indicated that on average 73.3% of the inputs came from net radiation and 25% from the direct lateral inflow net advection, while the outputs were mainly dominated by latent heat flux (73.2%) and sensible heat flux (25.1%). These results highlight the importance of the lateral inflow and the latent heat fluxes in the heat budget of a cascading reservoir system. From a monthly perspective, heat advection occurred mainly in summer due to higher upstream and lateral inflow temperatures than outflow temperatures. It confirms the importance of advection flows in the heat budget and the calculation of the turbulent heat fluxes.

The thermal phases of the reservoir varied in duration and timing. Reverse stratification lasted approximately 160 days, from mid-December to mid-May, while summer stratification lasted approximately 155 days, from mid-June to early November. These time intervals separated two mixing episodes, one in the spring that lasted about 22 days and one in the fall that lasted about 28 days. Surface and deep-water temperatures differed in time as well as in annual amplitude, with the with the maximum surface temperature observed in August, while deeper layers reached their maximum in September. The thermocline lasted on average 155 days, with a strong amplitude ΔT and a weak temperature gradient $\Delta T/\Delta z$ in August that inversed in September and October (weak amplitude and stronger temperature gradient).

Finally, during a period when water storage was drawn down for power production, the heat storage of the water column declined by 20% in response to the large removal of thermal mass from the reservoir. This highlighted the influence of the hydrological regime on the thermal structure of the reservoir. Water management governed variations in the thermocline, both in terms of depth and temperature, and ultimately changes in the energy balance, particularly turbulent fluxes that reflected the amount of heat stored in the reservoir. In sum, we showed that advective fluxes made a significant contribution to the reservoir's water and heat balances and should therefore not be ignored in climate modeling.

Acknowledgments. The authors would like to acknowledge Paul del Giorgio for sharing the Bernard River database. They are also grateful to Annie-Claude Parent, Dany Crépault, Denis Jobin, and Benjamin Bouchard for their contribution to this work. This research was funded by the Natural Sciences and Engineering Research Council of Canada (NSERC) through Grant RDCPJ508080-16 entitled "Observation and modelling of net evaporation from a boreal hydroelectric complex (water footprint)."

Data availability statement. Data are available upon request.

REFERENCES

Almeida, M. C., and Coauthors, 2022: Modeling reservoir surface temperatures for regional and global climate models: A

Brought to you by I.N.R.S. | Unauthenticated | Downloaded 03/14/24 01:14 PM UTC

multi-model study on the inflow and level variation effects. *Geosci. Model Dev.*, **15**, 173–197, https://doi.org/10.5194/gmd-15-173-2022.

Bashir, A., M. A. Shehzad, I. Hussain, M. I. A. Rehmani, and S. H. Bhatti, 2019: Reservoir inflow prediction by ensembling wavelet and bootstrap techniques to multiple linear regression model. *Water Resour. Manage.*, **33**, 5121–5136, https://doi.org/10.1007/s11269-019-02418-1.

Beck, H. E., N. E. Zimmermann, T. R. McVicar, N. Vergopolan, A. Berg, and E. F. Wood, 2018: Present and future Köppen-Geiger climate classification maps at 1-km resolution. *Sci. Data*, **5**, 180214, https://doi.org/10.1038/sdata.2018.214.

Birge, E. A., 1897: *Plankton Studies on Lake Mendota: The Crustacea of the Plankton, July, 1894–Dec., 1896. II.* Academic Press, 451 pp.

Blanken, P. D., and Coauthors, 2000: Eddy covariance measurements of evaporation from Great Slave Lake, Northwest Territories, Canada. *Water Resour. Res.*, **36**, 1069–1077, https://doi.org/10.1029/1999WR900338.

——, C. Spence, N. Hedstrom, and J. D. Lenters, 2011: Evaporation from Lake Superior: 1. Physical controls and processes. *J. Great Lakes Res.*, **37**, 707–716, https://doi.org/10.1016/j.jglr.2011.08.009.

Bolsenga, S. J., 1975: Estimating energy budget components to determine Lake Huron evaporation. *Water Resour. Res.*, **11**, 661–666, https://doi.org/10.1029/WR011i005p00661.

Bouin, M. N., and Coauthors, 2012: Using scintillometry to estimate sensible heat fluxes over water: First insights. *Bound.-Layer Meteor.*, **143**, 451–480, https://doi.org/10.1007/s10546-012-9707-8.

Çalışkan, A., and Ş. Elçi, 2009: Effects of selective withdrawal on hydrodynamics of a stratified reservoir. *Water Resour. Manage.*, **23**, 1257–1273, https://doi.org/10.1007/s11269-008-9325-x.

Cheng, B., F. Xie, P. Lu, P. Huo, and M. Leppäranta, 2021: The role of lake heat flux in the growth and melting of ice. *Adv. Polar Sci.*, **32**, 364–373, https://doi.org/10.13679/j.advps.2021.0051.

Denfeld, B. A., H. M. Baulch, P. A. del Giorgio, S. E. Hampton, and J. Karlsson, 2018: A synthesis of carbon dioxide and methane dynamics during the ice-covered period of northern lakes. *Limnol. Oceanogr. Lett.*, **3**, 117–131, https://doi.org/10.1002/lol2.10079.

DeWalle, D. R., and A. Rango, 2008: *Principles of Snow Hydrology*. Cambridge University Press, 410 pp.

Dirnberger, J. M., and J. Weinberger, 2005: Influences of lake level changes on reservoir water clarity in Allatoona Lake, Georgia. *Lake Reservoir Manage.*, **21**, 24–29, https://doi.org/10.1080/07438140509354409.

Elo, P., 2007: The energy balance and vertical thermal structure of two small boreal lakes in summer. *Boreal Environ. Res.*, **12**, 585–600.

Finkelstein, P. L., and P. F. Sims, 2001: Sampling error in eddy correlation flux measurements. *J. Geophys. Res.*, **106**, 3503–3509, https://doi.org/10.1029/2000JD900731.

Foken, T., 2008: The energy balance closure problem: An overview. *Ecol. Appl.*, **18**, 1351–1367, https://doi.org/10.1890/06-0922.1.

George, J., L. Janaki, and J. P. Gomathy, 2019: Prediction of daily reservoir inflow using atmospheric predictors. *Sustainable Water Resour. Manage.*, **5**, 1745–1754, https://doi.org/10.1007/s40899-019-00323-4.

Han, J.-C., and L. Wright, 2022: *Analytical Heat Transfer*. 2nd ed. CRC Press, 595 pp.

Harvey, R., L. Lye, A. Khan, and R. Paterson, 2011: The influence of air temperature on water temperature and the concentration of dissolved oxygen in Newfoundland Rivers. *Can. Water Resour. J.*, **36**, 171–192, https://doi.org/10.4296/cwrj3602849.

Heiskanen, J. J., and Coauthors, 2015: Effects of water clarity on lake stratification and lake-atmosphere heat exchange. *J. Geophys. Res. Atmos.*, **120**, 7412–7428, https://doi.org/10.1002/2014JD022938.

Hutchinson, G. E., and Y. H. Edmondson, 1957: *A Treatise on Limnology: Introduction to Lake Biology and the Limnoplankton*. J. Wiley, 3734 pp.

Hydro-Québec, 2007: *Vue d'Ensemble et Description des Aménagments. Complexe de la Romaine: Étude d'Impact sur l'Environnement*, Vol. 1, Hydro-Québec, 314 pp., https://www.hydroquebec.com/data/romaine/pdf/ei_volume01.pdf.

Jammet, M., P. Crill, S. Dengel, and T. Friborg, 2015: Large methane emissions from a subarctic lake during spring thaw: Mechanisms and landscape significance. *J. Geophys. Res. Biogeosci.*, **120**, 2289–2305, https://doi.org/10.1002/2015JG003137.

Juday, C., 1940: The annual energy budget of an inland lake. *Ecology*, **21**, 438–450, https://doi.org/10.2307/1930283.

Kallel, H., A. Thiboult, M. D. Mackay, D. F. Nadeau, and F. Anctil, 2024: Modeling heat and water exchanges between the atmosphere and an 85-km^2 dimictic subarctic reservoir using the 1D Canadian Small Lake Model. *J. Hydrometeor.*, https://doi.org/10.1175/JHM-D-22-0132.1, in press.

Kirillin, G., and Coauthors, 2012: Physics of seasonally ice-covered lakes: A review. *Aquat. Sci.*, **74**, 659–682, https://doi.org/10.1007/s00027-012-0279-y.

Koenings, J. P., and J. A. Edmundson, 1991: Secchi disk and photometer estimates of light regimes in Alaskan lakes: Effects of yellow color and turbidity. *Limnol. Oceanogr.*, **36**, 91–105, https://doi.org/10.4319/lo.1991.36.1.0091.

Leach, J. A., B. T. Neilson, C. A. Buahin, R. D. Moore, and H. Laudon, 2021: Lake Outflow and hillslope lateral inflows dictate thermal regimes of forested streams draining small lakes. *Water Resour. Res.*, **57**, e2020WR028136, https://doi.org/10.1029/2020WR028136.

Leppäranta, M., E. Lindgren, and K. Shirasawa, 2016: The heat budget of Lake Kilpisjärvi in the Arctic tundra. *Hydrol. Res.*, **48**, 969–980, https://doi.org/10.2166/nh.2016.171.

——, ——, L. Wen, and G. Kirillin, 2019: Ice cover decay and heat balance in Lake Kilpisjärvi in Arctic tundra: Ice decay in Lake Kilpisjärvi. *J. Limnol.*, **78**, 163–175, https://doi.org/10.4081/jlimnol.2019.1879.

Long, Y., H. Wang, C. Jiang, and S. Ling, 2019: Seasonal inflow forecasts using gridded precipitation and soil moisture information: Implications for reservoir operation. *Water Resour. Manage.*, **33**, 3743–3757, https://doi.org/10.1007/s11269-019-02330-8.

MacIntyre, S., J. R. Romero, G. M. Silsbe, and B. M. Emery, 2014: Stratification and horizontal exchange in Lake Victoria, East Africa. *Limnol. Oceanogr.*, **59**, 1805–1838, https://doi.org/10.4319/lo.2014.59.6.1805.

MacKay, M. D., 2012: A process-oriented small lake scheme for coupled climate modeling applications. *J. Hydrometeor.*, **13**, 1911–1924, https://doi.org/10.1175/JHM-D-11-0116.1.

——, and Coauthors, 2009: Modeling lakes and reservoirs in the climate system. *Limnol. Oceanogr.*, **54**, 2315–2329, https://doi.org/10.4319/lo.2009.54.6_part_2.2315.

Mahabbati, A., J. Beringer, M. Leopold, I. McHugh, J. Cleverly, P. Isaac, and A. Izady, 2021: A comparison of gap-filling

Brought to you by I.N.R.S. | Unauthenticated | Downloaded 03/14/24 01:14 PM UTC

algorithms for eddy covariance fluxes and their drivers. *Geosci. Instrum. Methods Data Syst.*, **10**, 123–140, https://doi.org/10.5194/gi-10-123-2021.

Mauder, M., M. Cuntz, C. Drüe, A. Graf, C. Rebmann, H. P. Schmid, M. Schmidt, and R. Steinbrecher, 2013: A strategy for quality and uncertainty assessment of long-term eddy-covariance measurements. *Agric. For. Meteor.*, **169**, 122–135, https://doi.org/10.1016/j.agrformet.2012.09.006.

——, and Coauthors, 2018: Evaluation of energy balance closure adjustment methods by independent evapotranspiration estimates from lysimeters and hydrological simulations. *Hydrol. Processes*, **32**, 39–50, https://doi.org/10.1002/hyp.11397.

Metzger, J., M. Nied, U. Corsmeier, J. Kleffmann, and C. Kottmeier, 2018: Dead Sea evaporation by eddy covariance measurements vs. aerodynamic, energy budget, Priestley–Taylor, and Penman estimates. *Hydrol. Earth Syst. Sci.*, **22**, 1135–1155, https://doi.org/10.5194/hess-22-1135-2018.

Miller, S. D., T. S. Hristov, J. B. Edson, and C. A. Friehe, 2008: Platform motion effects on measurements of turbulence and air–sea exchange over the open ocean. *J. Atmos. Oceanic Technol.*, **25**, 1683–1694, https://doi.org/10.1175/2008JTECHO547.1.

Momii, K., and Y. Ito, 2008: Heat budget estimates for Lake Ikeda, Japan. *J. Hydrol.*, **361**, 362–370, https://doi.org/10.1016/j.jhydrol.2008.08.004.

Moreno-Ostos, E., R. Marcé, J. Ordóñez, J. Dolz, and J. Armengol, 2008: Hydraulic management drives heat budgets and temperature trends in a Mediterranean reservoir. *Int. Rev. Hydrobiol.*, **93**, 131–147, https://doi.org/10.1002/iroh.200710965.

Nazemi, A., and H. S. Wheater, 2015: On inclusion of water resource management in Earth system models—Part 2: Representation of water supply and allocation and opportunities for improved modeling. *Hydrol. Earth Syst. Sci.*, **19**, 63–90, https://doi.org/10.5194/hess-19-63-2015.

Nordbo, A., S. Launiainen, I. Mammarella, M. Lepparanta, J. Huotari, A. Ojala, and T. Vesala, 2011: Long-term energy flux measurements and energy balance over a small boreal lake using eddy covariance technique. *J. Geophys. Res.*, **116**, D02119, https://doi.org/10.1029/2010JD014542.

Olsson, F., 2022: Impacts of water residence time on lake thermal structure: Implications for management and climate change. Ph.D. dissertation, Lancaster University, 271 pp.

——, and Coauthors, 2022: Annual water residence time effects on thermal structure: A potential lake restoration measure? *J. Environ. Manage.*, **314**, 115082, https://doi.org/10.1016/j.jenvman.2022.115082.

Oswald, C. J., and W. R. Rouse, 2004: Thermal characteristics and energy balance of various-size Canadian Shield lakes in the Mackenzie River basin. *J. Hydrometeor.*, **5**, 129–144, https://doi.org/10.1175/1525-7541(2004)005<0129:TCAEBO>2.0.CO;2.

Parajuli, A., D. F. Nadeau, F. Anctil, and M. Alves, 2021: Multilayer observation and estimation of the snowpack cold content in a humid boreal coniferous forest of eastern Canada. *Cryosphere*, **15**, 5371–5386, https://doi.org/10.5194/tc-15-5371-2021.

Patel, S. S., and A. J. Rix, 2019: Water surface albedo modelling for floating PV plants. *Sixth Southern African Solar Energy Conference (SASEC)*, Port Alfred, South Africa, Nelson Mandela University, 8, https://www.sasec.org.za/papers2019/8.pdf.

Pierre, A., P.-E. Isabelle, D. F. Nadeau, A. Thiboult, A. Perelet, A. N. Rousseau, F. Anctil, and J. Deschamps, 2022: Estimating sensible and latent heat fluxes over an inland water body using optical and microwave scintillometers. *Bound.-Layer Meteor.*, **185**, 277–308, https://doi.org/10.1007/s10546-022-00732-7.

——, D. F. Nadeau, A. Thiboult, A. N. Rousseau, A. Tremblay, P.-E. Isabelle, and F. Anctil, 2023: Characteristic time scales of evaporation from a subarctic reservoir. *Hydrol. Processes*, **37**, e14842, https://doi.org/10.1002/hyp.14842.

Ragotzkie, R. A., 1978: Heat budgets of lakes. *Lakes, Chemistry, Geology and Physics*, A. Lerman, Ed., Springer, 1–19, https://doi.org/10.1007/978-1-4757-1152-3_1.

——, and G. E. Likens, 1964: The heat balance of two Antarctic lakes. *Limnol. Oceanogr.*, **9**, 412–425, https://doi.org/10.4319/lo.1964.9.3.0412.

Read, J. S., D. P. Hamilton, I. D. Jones, K. Muraoka, L. A. Winslow, R. Kroiss, C. H. Wu, and E. Gaiser, 2011: Derivation of lake mixing and stratification indices from high-resolution lake buoy data. *Environ. Modell. Software*, **26**, 1325–1336, https://doi.org/10.1016/j.envsoft.2011.05.006.

Reichstein, M., and Coauthors, 2005: On the separation of net ecosystem exchange into assimilation and ecosystem respiration: Review and improved algorithm. *Global Change Biol.*, **11**, 1424–1439, https://doi.org/10.1111/j.1365-2486.2005.001002.x.

Rodríguez-Rodríguez, M., and E. Moreno-Ostos, 2006: Heat budget, energy storage and hydrological regime in a coastal lagoon. *Limnologica*, **36**, 217–227, https://doi.org/10.1016/j.limno.2006.05.003.

——, ——, I. De Vicente, L. Cruz-Pizarro, and S. L. R. Da Silva, 2004: Thermal structure and energy budget in a small high mountain lake: La Caldera, Sierra Nevada, Spain. *N. Z. J. Mar. Freshwater Res.*, **38**, 879–894, https://doi.org/10.1080/00288330.2004.9517287.

Rouse, W. R., C. Oswald, J. Binyamin, P. D. Blanken, W. M. Schertzer, and C. Spence, 2003: Interannual and seasonal variability of the surface energy balance and temperature of central Great Slave Lake. *J. Hydrometeor.*, **4**, 720–730, https://doi.org/10.1175/1525-7541(2003)004<0720:IASVOT>2.0.CO;2.

——, ——, ——, C. Spence, W. M. Schertzer, P. D. Blanken, N. Bussières, and C. R. Duguay, 2005: The role of northern lakes in a regional energy balance. *J. Hydrometeor.*, **6**, 291–305, https://doi.org/10.1175/JHM421.1.

Saros, J. E., R. M. Northington, C. L. Osburn, B. T. Burpee, and N. John Anderson, 2016: Thermal stratification in small arctic lakes of southwest Greenland affected by water transparency and epilimnetic temperatures. *Limnol. Oceanogr.*, **61**, 1530–1542, https://doi.org/10.1002/lno.10314.

Saur, J. F. T., and E. R. Anderson, 1956: The heat budget of a body of water of varying volume. *Limnol. Oceanogr.*, **1**, 247–251, https://doi.org/10.4319/lo.1956.1.4.0247.

Schmid, M., and J. Read, 2022: Heat Budget of Lakes. *Encyclopedia of Inland Waters*, 2nd ed. T. Mehner and K. Tockner, Eds., Elsevier Science, 467–473.

Seibert, J., M. Jenicek, M. Huss, T. Ewen, and D. Viviroli, 2021: Snow and ice in the hydrosphere. *Snow and Ice-Related Hazards, Risks, and Disasters*, 2nd ed. W. Haeberli, J. F. Shroder, and C. Whiteman, Eds., Elsevier Science, 93–135.

Spank, U., M. Hehn, P. Keller, M. Koschorreck, and C. Bernhofer, 2020: A season of eddy-covariance fluxes above an extensive water body based on observations from a floating platform. *Bound.-Layer Meteor.*, **174**, 433–464, https://doi.org/10.1007/s10546-019-00490-z.

Spence, C., W. R. Rouse, D. Worth, and C. Oswald, 2003: Energy budget processes of a small northern lake. *J. Hydrometeor.*,

Brought to you by I.N.R.S. | Unauthenticated | Downloaded 03/14/24 01:14 PM UTC

4, 694–701, https://doi.org/10.1175/1525-7541(2003)004<0694:EBPOAS>2.0.CO;2.

Subin, Z. M., W. J. Riley, and D. Mironov, 2012: An improved lake model for climate simulations: Model structure, evaluation, and sensitivity analyses in CESM1. *J. Adv. Model. Earth Syst.*, **4**, M02001, https://doi.org/10.1029/2011MS000072.

Vallet-Coulomb, C., D. Legesse, F. Gasse, Y. Travi, and T. Chernet, 2001: Lake evaporation estimates in tropical Africa (Lake Ziway, Ethiopia). *J. Hydrol.*, **245** (1–4), 1–18, https://doi.org/10.1016/S0022-1694(01)00341-9.

Venkateshan, S. P., 2021: *Heat Transfer*. 3rd ed. Springer, 1015 pp.

Vincent, W. F., S. MacIntyre, R. H. Spigel, and I. Laurion, 2008: The physical limnology of high-latitude lakes. *Polar Lakes and Rivers; Limnology of Arctic and Antarctic Aquatic Ecosystems*, Oxford University Press, 65–82.

Wilson, K., and Coauthors, 2002: Energy balance closure at FLUXNET sites. *Agric. For. Meteor.*, **113**, 223–243, https://doi.org/10.1016/S0168-1923(02)00109-0.

Winter, T. C., D. C. Buso, D. O. Rosenberry, G. E. Likens, A. J. M. Sturrock, and D. P. Mau, 2003: Evaporation determined by the energy-budget method for Mirror Lake, New Hampshire. *Limnol. Oceanogr.*, **48**, 995–1009, https://doi.org/10.4319/lo.2003.48.3.0995.

Xing, Z., D. A. Fong, K. M. Tan, E. Y.-M. Lo, and S. G. Monismith, 2012: Water and heat budgets of a shallow tropical reservoir. *Water Resour. Res.*, **48**, W06532, https://doi.org/10.1029/2011WR011314.

Brought to you by I.N.R.S. | Unauthenticated | Downloaded 03/14/24 01:14 PM UTC